TOI-837 b is a young Saturn-sized exoplanet with a massive 70 M core

Barragán, Oscar; Yu, Haochuan; Freckelton, Alix Violet; Meech, Annabella; Cretignier, Michael; Mortier, Annelies; Aigrain, Suzanne; Klein, Baptiste; O'Sullivan, Niamh K; Gillen, Edward; Nielsen, Louise Dyregaard; Mallorquin, Manuel; Zicher, Norbert

[Link to publication on Research at Birmingham portal](#)

TOI-837 b is a young Saturn-sized exoplanet with a massive 70 M$_\oplus$ core

Oscar Barragán [ORCID],[1]* Haochuan Yu [ORCID],[1] Alix Violet Freckelton [ORCID],[2] Annabella Meech [ORCID],[3] Michael Cretignier [ORCID],[1] Annelies Mortier [ORCID],[2] Suzanne Aigrain,[1] Baptiste Klein [ORCID],[1] Niamh K. O'Sullivan,[1] Edward Gillen [ORCID],[4] Louise Dyregaard Nielsen [ORCID],[5] Manuel Mallorquín[6,7] and Norbert Zicher[1]

[1]*Sub-department of Astrophysics, Department of Physics, University of Oxford, Oxford OX1 3RH, UK*
[2]*School of Physics and Astronomy, University of Birmingham, Edgbaston, Birmingham B15 2TT, UK*
[3]*Center for Astrophysics, Harvard & Smithsonian, 60 Garden St, Cambridge, MA 02138, USA*
[4]*Astronomy Unit, Queen Mary University of London, Mile End Road, London E1 4NS, UK*
[5]*University Observatory Munich, Ludwig Maximilian University, Scheinerstrasse 1, D-81679 Munich, Germany*
[6]*Instituto de Astrofísica de Canarias (IAC), Calle Vía Láctea s/n, E-38205 La Laguna, Tenerife, Spain*
[7]*Departamento de Astrofísica, Universidad de La Laguna (ULL), E-38206 La Laguna, Tenerife, Spain*

ABSTRACT

We present an exhaustive photometric and spectroscopic analysis of TOI-837, a F9/G0 35 Myr young star, hosting a transiting exoplanet, TOI-837 b, with an orbital period of $\sim$8.32 d. Utilizing data from the *Transiting Exoplanet Survey Satellite* and ground-based observations, we determine a planetary radius of $0.818^{+0.034}_{-0.024}$ R_J for TOI-837 b. Through detailed High Accuracy Radial Velocity Planet Searcher spectroscopic time series analysis, we derive a Doppler semi-amplitude of $34.7^{+5.3}_{-5.6}$ m s^{-1}, corresponding to a planetary mass of $0.379^{+0.058}_{-0.061}$ M_J. The derived planetary properties suggest a substantial core of approximately 70 M$_\oplus$, constituting about 60 per cent of the planet's total mass. This finding poses a significant challenge to existing theoretical models of core formation. We propose that future atmospheric observations with *JWST* could provide insights into resolving ambiguities of TOI-837 b, offering new perspectives on its composition, formation, and evolution.

Key words: techniques: photometric – techniques: radial velocities – planets and satellites: individual: TOI-837 – stars: activity.

1 INTRODUCTION

Characterizing the properties of young exoplanets (<1 Gyr) at different stages is crucial to understanding the evolution and populations of exoplanets. These planets are often elusive to detection using indirect techniques like transit and radial velocity (RV) methods, as strong stellar activity generates stellar signals that often overshadows their signals in photometric and spectroscopic data. Recently, tens of young transiting exoplanets have been discovered (e.g. David et al. 2018; Bouma et al. 2020; Rizzuto et al. 2020; Hobson et al. 2021; Martioli et al. 2021; Barragán et al. 2022b; Mann et al. 2022). This success is largely attributed to missions like *K2* (Howell et al. 2014) and the *Transiting Exoplanet Survey Satellite* (*TESS*; Ricker et al. 2015) that provide thousands of light curves of young stars.

After identifying a young transiting exoplanet, the next step typically involves spectroscopic observations to observe the star's RV variations caused by the planet to measure its mass. However, separating signals from the planet and star in RV data remains challenging. Gaussian processes (GPs) have emerged as a favoured method for modelling activity-induced radial velocities, offering a flexible way to represent stochastic variations, such as the quasi-periodic (QP) stellar signals (see e.g. Aigrain & Foreman-Mackey

2023). Multiple authors have used GPs, and variations of them such as multidimensional GPs (see e.g. Rajpaul et al. 2015; Barragán et al. 2022a), to detect RV planetary signals on spectroscopic time series of active young stars (e.g. Barragán et al. 2019b, 2023; Zicher et al. 2022; Mallorquín et al. 2023; Mantovan et al. 2024). Nevertheless, although widely embraced by the community, there exists a notable concern that the GP activity model may inadvertently mask or alter potential planetary signals (see e.g. discussions in Ahrer et al. 2021; Rajpaul et al. 2021). A recent example of this comes from Suárez Mascareño et al. (2021). The authors, utilizing GPs, discovered that the planets orbiting the young V1298 Tauri exhibited significantly higher density than anticipated. However, these detections have been challenged by the exoplanet community. Blunt et al. (2023) suggested that Suárez Mascareño et al. (2021)'s detections may have been affected by overfitting, thereby questioning the reliability of their RV Doppler detections. This is crucial, especially in cases where the measurements are in tension with models.

Bouma et al. (2020, hereafter B20) reported the discovery and validation of the young transiting exoplanet around TOI-837. The star is a young ($\sim$35 Myr) F9/G0 dwarf star in the southern open cluster IC 2602. TOI-837's main identifiers and parameters are given in Table 1. They used *TESS* Cycle 1, the *Gaia* mission, multiband photometry, and spectroscopic observations to validate the planetary nature of a transit signal. The transit object corresponds to a planet with a radius of $\sim$0.77 R_J and a period of 8.32 d. In this paper, we present a spectroscopic follow-up and exhaustive analysis of TOI-

Table 1. Main identifiers and parameters for TOI-837.

Parameter	Value	Source
Main identifiers		
Gaia DR3	5251 470 948 229 949 568	Gaia Collaboration (2021)
TYC	8964-17-1	Høg et al. (2000)
2MASS	J10280898-6430189	Cutri et al. (2003)
Spectral type	F9/G0	Bouma et al. (2020)
Equatorial coordinates, proper motion, and parallax		
α (J2000.0)	10:28:08.9903	Gaia Collaboration (2021)
δ (J2000.0)	-64:30:18.9364	Gaia Collaboration (2021)
μ_α (mas yr^{-1})	-17.912 ± 0.014	Gaia Collaboration (2021)
μ_δ (mas yr^{-1})	11.490 ± 0.014	Gaia Collaboration (2021)
π (mas)	7.0108 ± 0.0124	Gaia Collaboration (2021)
Distance (pc)	142.74 ± 0.25	Gaia Collaboration (2021)
Magnitudes		
B	11.12 ± 0.06	Høg et al. (2000)
V	10.64 ± 0.05	Høg et al. (2000)
Gaia	10.3598 ± 0.0028	Gaia Collaboration (2021)
J	9.392 ± 0.030	Cutri et al. (2003)
H	9.108 ± 0.038	Cutri et al. (2003)
K_s	8.933 ± 0.026	Cutri et al. (2003)
$W1$	8.901 ± 0.023	*AllWISE*
$W2$	8.875 ± 0.021	*AllWISE*
$W3$	8.875 ± 0.020	*AllWISE*
Stellar parameters		
$T_{\rm eff}$ (K)	5995 ± 79	This work
$\log g_{\rm spec}$ (cgs)	4.61 ± 0.08	This work
[Fe/H]	0.01 ± 0.04	This work
$v \sin i$ (km s^{-1})	16.8 ± 0.1	This work
Mass (M$_\odot$)	$1.142^{+0.008}_{-0.011}$	This work
Radius (R$_\odot$)	$1.052^{+0.012}_{-0.007}$	This work
Luminosity (L$_\odot$)	$1.34^{+0.06}_{-0.12}$	This work
Density (g cm^{-3})	$1.38^{+0.02}_{-0.04}$	This work
$\log g_{\rm isoc}$ (cgs)	$4.453^{+0.003}_{-0.008}$	This work
Age (Myr)	35^{+7}_{-4}	This work
$P_{\rm rot,max}$ (d)	3.17 ± 0.04	This work

837 to characterize further the nature of TOI-837 b. This paper is structured as follows. The photometric and spectroscopic data of TOI-837 are detailed in Section 2. The analytical methods applied to this data are outlined in Section 3. A discussion of the findings is provided in Section 4, and the paper concludes with a summary of the key outcomes in Section 5. We acknowledge that while this paper was being reviewed, we learned that Damasso et al., (2024) were performing an independent analysis of the public HARPS data of TOI-837. Should the reader wish to compare their results with ours, it would serve to further validate/test the findings presented in this manuscript.

2 TOI-837 DATA

2.1 *TESS* data

TOI-837 (TIC 460205581) was observed by the *TESS* mission on Cycles 1, 3, and 5. During Cycle 1, TOI-837 was observed in Sectors 10 and 11 from 2019 March 26 to 2019 May 20 with a 2 min cadence. The *TESS* Science Processing Operations Center (SPOC; Jenkins et al. 2016) transit search (Jenkins 2002; Jenkins et al. 2010, 2020) discovered a transiting signal with a period of 8.3 d in TOI-837's light curve. This was announced in the *TESS* SPOC Data Validation Report (DVR; Twicken et al. 2018; Li et al. 2019) and designated by

the *TESS* Science Office as *TESS* Object of Interest (TOI; Guerrero et al. 2021) TOI-837.01 (hereafter TOI-837 b).

It should be noted that TOI-837 is situated in a relatively dense stellar region. Utilizing *Gaia* Data Release 2 (DR2) data, B20 identified two sources brighter than $T = 16$ within the same *TESS* pixel as TOI-837: TIC 847769574 ($T = 14.6$), which was argued a possible comoving companion within the IC 2602 moving group, and TIC 460205587 ($T = 13.1$), a background giant star. B20 employed speckle imaging and photometric ground-based observations (refer to Section 2.2) to rule out potential false-positive scenarios and confirm that the observed transits occur on TOI-837, thereby validating the planetary nature of the transiting signal. More recently, Behmard, Dai & Howard (2022), using *Gaia* Data Release 3 (DR3) data, suggested that TIC 847769574 is likely gravitational bound to TOI-837. This companion is consistent with being an M dwarf, with an estimated mass of 0.393 ± 0.034 M$_\odot$ and a projected separation of approximately 330 au, suggesting that the TOI-837 system may be binary, with TIC 847769574 being TOI-837 (B). However, the findings from B20 continue to support the scenario of the planet transiting TOI-837 (A). For simplicity, this paper will continue to refer to the planet as TOI-837 b instead of TOI-837 (A) b. We note that any extra flux coming from contaminating stars within *TESS* pixels (named crowding) is corrected for the Pre-search Data Conditioning Simple Aperture Photometry (PDCSAP) light curves by the SPOC (Stumpe et al. 2012). Therefore, no further processing is needed for the analyses in this paper where we use PDCSAP light curves.

During Cycles 3 and 5, TOI-837 was reobserved in Sectors 37 and 38 (from 2021 April 2 to 2021 May 26, with 2 min cadence) and Sectors 63 and 64 (2023 March 10 to 2023 May 4, with 20 s cadence), respectively. We downloaded the PDCSAP (Smith et al. 2012; Stumpe et al. 2012, 2014) light curves for TOI-837 from the Mikulski Archive for Space Telescopes (MAST). Fig. 1 shows the TOI-837's light curves for all the three *TESS* cycles. TOI-837 will be reobserved by *TESS* in Sector 90 during the first semester of 2025.

To perform the transit analysis we flattened the *TESS* light curves (see Section 3.2). The *TESS* light curves for TOI-837 exhibit variations outside of transits, possibly due to stellar or instrumental variability. The *TESS* light curves were detrended using the open-source code CITLALICUE (https://https://github.com/oscaribv/citlalicue; Barragán et al. 2022a). In essence, CITLALICUE employs GPs, as implemented in GEORGE (Ambikasaran et al. 2015), to model light-curve fluctuations outside of transits. We provided CITLALICUE with normalized light curves and the ephemeris for the transit signal. To focus on removing low-frequency signals, we used data binned at 3-h intervals and masked all transits when fitting the GP with a QP kernel (as in Ambikasaran et al. 2015). We applied an iterative maximum likelihood optimization coupled with a 5σ clipping technique to identify the best model for light-curve variations outside of transits. Subsequently, we divided the entire light curves based on this model, resulting in a flattened curve showing only transit signals. It is worth noting that each *TESS* cycle was detrended individually. The detrended light curves for all *TESS* cycles are presented in Fig. 1.

2.2 Ground-based photometric data

B20 performed multiband ground-based follow-up of TOI-837. For full details on the acquisition and reduction, we refer the reader to that paper. Four transit events were monitored using the 0.36-m telescope at El Sauce Observatory, situated in Chile's Río Hurtado Valley. The data collection occurred during specific nights: the Cousins *R* band
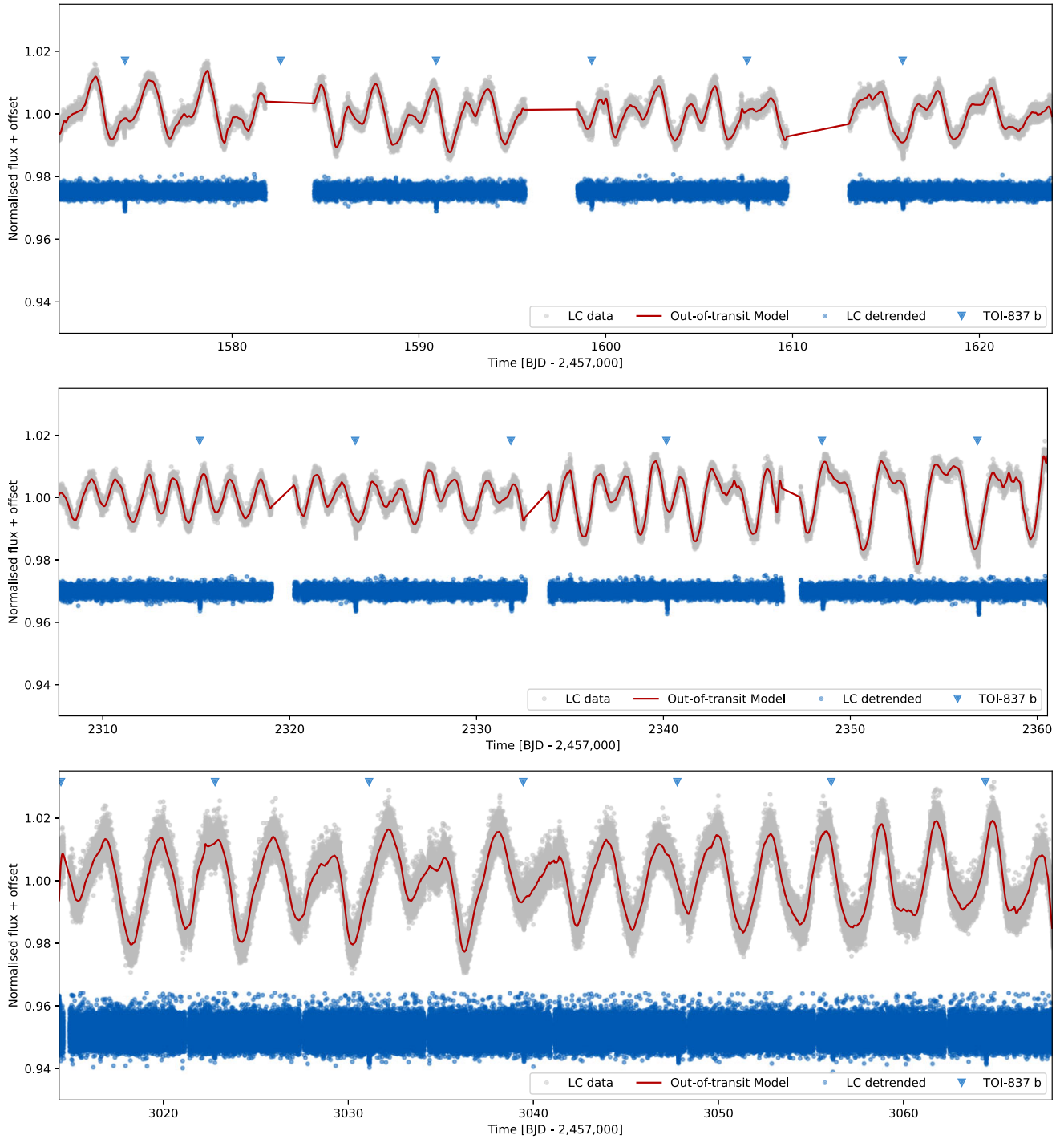
Figure 1. *TESS* light curves for TOI-837 in Cycles 1, 3, and 5 (from top to bottom). *TESS* data are shown with light grey points with the out-of-transit variability model overplotted with a red line. The resulting flattened light curve is presented with blue points. TOI-837's transit positions are marked with a blue triangle. All plots have the same *y* range to ease the comparison of data and signals.

was used on 2020 April 1 and 26, the Cousins *I* band on 2020 May 21, and the Johnson *B* band on 2020 June 14. TOI-837 was also observed by the Antarctic Search for Transiting ExoPlanets (ASTEP) telescope at the Concordia base on the Antarctic Plateau, on the dates of 2020 May 12, May 29, June 14, and June 23. We downloaded all these public data to include them in our analyses.

2.3 HARPS spectroscopic observations

We acquired 75 high-resolution ($R \approx 115\,000$, wavelength range of 380–690 nm) spectra of TOI-837 with the High Accuracy Radial Velocity Planet Searcher (HARPS; Mayor et al. 2003) spectrograph. The instrument is mounted at the 3.6-m ESO telescope at La Silla Observatory, Chile.

Table 2. HARPS spectroscopic measurements. The full version of this table is available in a machine-readable format as part of the supplementary material.

Time (BJD$_{\rm TDB}$ − 247 0000)	RV (km s^{-1})	RV GND (km s^{-1})	RV GND_2.8 (km s^{-1})	$\sigma_{\rm RV}$ (km s^{-1})	FWHM (km s^{-1})	$\sigma_{\rm FWHM}$ (km s^{-1})	BIS (km s^{-1})	$\sigma_{\rm BIS}$ (km s^{-1})	$S_{\rm HK}$	$\sigma_{S_{\rm HK}}$	Hα	$\sigma_{\rm H\alpha}$
2855.882062	0.0634	0.0497	0.0519	0.0160	24.0112	0.0521	− 0.0708	0.0216	0.0386	0.0242	0.3979	0.0039
2859.873603	− 0.0075	− 0.0169	− 0.0167	0.0155	23.8725	0.0505	− 0.0957	0.0210	0.0811	0.0238	0.3918	0.0035
2860.880897	0.0386	− 0.0272	− 0.0248	0.0206	23.7631	0.0671	− 0.4361	0.0278	0.0255	0.0347	0.3972	0.0048
2861.882173	0.1588	0.1126	0.1105	0.0172	24.0269	0.0560	− 0.3255	0.0232	0.0683	0.0302	0.3954	0.0041
2863.879982	0.0442	− 0.0012	− 0.0020	0.0152	23.9185	0.0493	− 0.3695	0.0204	− 0.0254	0.0214	0.3899	0.0031
...	...	...	...	...	...	...	...	...	...	...	...	...

The observations were carried out between 2022 October 3 and 2023 January 16, as part of the observing program 0110.C-4341(A) (PI: Yu). The typical exposure time per observation was 1800 s, except for the observations before October 25 where the exposure time was set to 900 s. This produced spectra with a typical signal-to-noise ratio (S/N) of 50 (30 for the 900 s exposures) at 550 nm.

We post-processed the 1D spectra produced by the official data reduction software (DRS). All the spectra $S(\lambda_i, t)$ were first continuum normalized by RASSINE (https://https://github.com/MichaelCretignier/Rassine_public; Cretignier et al. 2020b), an upper envelope method fitting the spectra continua $C(\lambda_i, t)$. The normalized spectra time series $f(\lambda_i, t) = S(\lambda_i, t)/C(\lambda_i, t)$ were then post-processed by YARARA (Cretignier et al. 2021). Given the limited S/N of the observations, we restricted the cleaning by YARARA to cosmic rays and tellurics that are the only notable features at such a level of flux precision. From this step onwards, four observations were rejected by YARARA based on an anomalous number of detected outliers. Those spectra were all very low S/N observations (<25). Once spectra were corrected of systematics, the normalized flux spectra $f(\lambda_i)$ were scaled back to absolute flux units spectra $S(\lambda_i)$ by using a reference continuum[1] $C_{\rm ref}(\lambda)$ where the bolometric flux of the spectra was preserved during the scaling:

$$S(\lambda_i, t) = f(\lambda_i, t)\, C_{\rm ref}(\lambda_i)\, \frac{\sum_i C(\lambda_i)}{\sum_i C_{\rm ref}(\lambda_i)}.$$

This step is equivalent in practice to the colour correction usually performed on the order-by-order cross-correlation functions (CCFs) to remove any dependency with airmass or weather condition (Lovis 2007; Cretignier 2022). We extracted the RVs and activity indicators by a Gaussian fit on CCFs obtained using the G2 mask of the HARPS DRS since for fast-rotating stars, the empirical line list (see e.g. Cretignier et al. 2020a) obtained from the observations could be imperfect due to a large number of blends. The full width at half-maximum (FWHM) of the CCFs shows a consequent broadening with a value around FWHM ~ 26 km s^{-1} in agreement with the fast rotation rate of the star (see Section 3.1). Since the CCFs are considerably broadened, we also extracted the RVs with a generalized normal distribution (GND) as introduced in Heitzmann et al. (2021). GND has for advantage to contains an extra shape parameter β that affects the kurtosis of the profile in order to produce a more 'top-hat flatten' behaviour. When $\beta = 2$, GND is fully equivalent to a Gaussian. We extracted the RVs using both a completely free GND model ($\beta(t)$ time dependent) and a more rigid one with the shape parameter β fixed to the mean value ($\beta(t) = 2.8$). The RVs obtained with these alternative parametrizations are fully consistent with the RVs obtained with the Gaussian fit. Our HARPS RV measurements have a typical error of 10 m s^{-1} and an rms of 100 m s^{-1}. Table 2 lists the extracted HARPS RV, RV GND, RV GND_2.8, FWHM, bisector

span (BIS), calcium lines S-index ($S_{\rm HK}$), and hydrogen-alpha (Hα) time series.

2.3.1 Periodograms

As a first check to test the information contained in our HARPS spectroscopic time series, we ran a general Lomb–Scargle (GLS; Zechmeister & Kürster 2009) periodogram on them. Fig. 2 shows the periodogram of all the time series. We can see that all of the spectroscopic time series peak around 3 and 1.5 d, which correspond to the rotational period of the star and its first harmonic. The peaks at the stellar rotation period and its first harmonic suggest the presence of active regions on the stellar surface (e.g. Aigrain, Pont & Zucker 2012). No substantial peak corresponding to the orbital period of TOI-837 b is evident in the raw RVs. We also check for signals at longer periods (up to 100 d, not shown in Fig. 2) and did not find any significant peak in any time series.

3 DATA ANALYSIS

3.1 Stellar parameters

3.1.1 Atmospheric parameters

We used the HARPS spectra to derive the atmospheric parameters of TOI-837. As this star is a fast rotator, we analysed the spectra using spectral synthesis. Two different methods were employed, FASMA-SYNTHESIS[2] and PAWS,[3] as well as two different sets of spectra, the DRS spectra and the YARARA-processed spectra (see Section 2.3). Each set of spectra was shifted in the lab frame and coadded and the analyses were performed on this coadded spectrum.

FASMA-SYNTHESIS made use of the MARCS atmospheric models (Gustafsson et al. 2008) and the radiative transfer code MOOG[4] micro- and macroturbulent velocities were calculated through the calibration relations mentioned in Tsantaki et al. (2013) and Doyle et al. (2014), respectively. More details on this method can be found in Tsantaki, Andreasen & Teixeira (2020).

PAWS uses the functionalities from ISPEC (Blanco-Cuaresma 2019) and is described in more detail in Freckelton et al. (2024). We used the Kurucz atmospheric models in our analysis (Kurucz 1993) and skipped the initial step of the equivalent width analysis as this is less reliable for fast rotators where the spectral lines are broadened.

These four analyses provided values for the effective temperature, the surface gravity, the metallicity, and the projected rotational velocity. All values are in agreement with their 1σ errors. For our adopted parameters, listed in Table 1, we choose to take a weighted average of all the results. The high value of the projected rotational

---

[1]Sometimes referred as a 'reference colour'.

[2]https://github.com/MariaTsantaki/FASMA-synthesis
[3]https://github.com/alixviolet/PAWS
[4]https://www.as.utexas.edu/~chris/moog.html
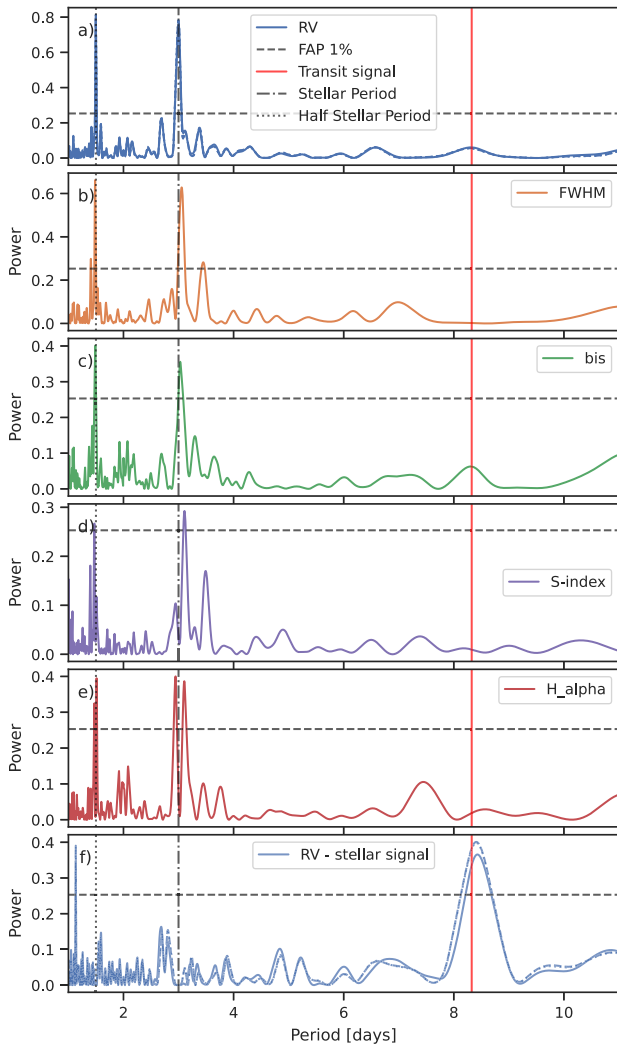
Figure 2. GLS periodograms of the spectroscopic time series. GLS periodograms of the spectroscopic time series are presented in panels (a) to (f). Panel (a) displays periodograms for Gaussian (solid line), GND (dotted line), and GND_2.8 (dashed line) extracted RVs, which appear overlapped. Panel (f) depicts a GLS periodogram for these RVs after removing the stellar model (see Section 3.4). The horizontal dashed line indicates the 1 per cent false alarm probability (FAP). The dot–dashed and dotted black lines represent the stellar rotation period and its first harmonic, respectively, while the vertical red line marks the orbital period of TOI-837 b.

velocity (16.8 km s^{-1}) confirms the fast-rotating nature of TOI-837. All other parameters are close to solar values.

3.1.2 Mass, radius, and age

To calculate the fundamental stellar parameters, we made use of the ISOCHRONES (Morton 2015) package. Our stellar models came from the MESA Isochrones and Stellar Tracks (MIST; Dotter 2016) and we used the nested sampler MULTINEST (Feroz et al. 2019) for our likelihood analysis. As input data, we used the photometric magnitudes B, V, J, H, K_s, $W1$, $W2$, $W3$, the *Gaia* DR3 parallax, and the spectroscopically derived effective temperature and metallicity. In a similar way as described in Mortier et al. (2020), we ran the code four times, each time changing the spectroscopic input to the individually obtained results and keeping the other data the same.

Narrow bounds were set on the stellar age, between 30 and 46 Myr, following B20, which helps constrain the stellar mass given strong correlations between mass and age for young stars.

After checking that all parameters from the individual runs agreed within errors, the final parameters and errors, listed in Table 1, were obtained from the median and 16th/84th percentile of the combined posterior distributions of the four runs. The mass and radius values are, unsurprisingly, close to solar values. From these, we can recalculate a much more precise value of the surface gravity. It is lower than, but consistent with, the spectroscopically derived surface gravity. Using the stellar radius and the projected rotational velocity, we can furthermore also place an upper limit on the stellar rotation period. We find that the rotation period has a maximum value of 3.17 ± 0.04 d. This is fully compatible with the values obtained with *TESS* and spectroscopic time series (see Section 3.3).

3.2 Transit analysis

For all the subsequent planet analyses we used the code PYANETI (https://https://github.com/oscaribv/pyaneti; Barragán, Gandolfi & Antoniciello 2019a; Barragán et al. 2022a). In all our runs we sample the parameter space with 250 walkers using the Markov chain Monte Carlo (MCMC) ensemble sampler algorithm implemented in PYANETI (Barragán et al. 2019a), which is based on Foreman-Mackey et al. (2013). The posterior distributions are created with the last 5000 iterations of converged chains. We thinned our chains by a factor of 10 giving a distribution of 125 000 points for each sampled parameter.

To speed up the transit modelling, we only model data chunks spanning a maximum of 3 h on either side of each transit mid-time. *TESS* and ground-based photometry were acquired with short cadence (<2 min). Therefore, we can assume that this data can be described by instantaneous evaluations of the transit models and we do not need model resampling (see e.g. Gandolfi et al. 2018). In total we have six different photometric data sets named: *TESS* 2 min data (Cycles 1 and 3), *TESS* 25 s data (Cycle 5), ASTEP, and El Sauce R, I, and B bands.

To model the transits of TOI-837 b, we need to set priors for the following set of parameters: time of mid-transit, T_0; orbital period, P_{orb}; orbital eccentricity, e, and angle of periastron, ω, using the polar parametrization $\sqrt{e}\cos\omega_\star$ and $\sqrt{e}\sin\omega_\star$; scaled planetary radius, $R_p/R_\star$; the stellar density, $\rho_\star$; and the limb darkening parameters q_1 and q_2 for each band (following Mandel & Agol 2002; Kipping 2013 models and parametrizations). We assume a black object transit and we sample for a single $R_p/R_\star$ for all bands (B20 showed that there is no variation of $R_p/R_\star$ in different bands). The scaled semimajor axis, $a/R_\star$, is recovered from $\rho_\star$ and Kepler's third law (see e.g. Winn 2010). The model also includes a photometric jitter term per data set to penalize the likelihood. We start by assuming that the orbit is circular, so we fix $\sqrt{e}\cos\omega_\star = \sqrt{e}\sin\omega_\star = 0$. For the rest of parameters, we set wide informative uniform priors as listed in Table 3.

To start our transit analysis, it is worth mentioning that TOI-837 b's transit looks V shaped, indicating that the transit could be grazing (where the grazing condition is given when $b > 1 - R_p/R_\star$). B20 reported $b = 0.94 \pm 0.013$ and $R_p/R_\star = 0.08 \pm 0.01$, suggesting that the transit is either grazing or nearly grazing. We note that B20 performed this analysis using the available data at the time: *TESS* Cycle 1 and the ground-based data. We performed an analysis using exactly this data set, and we obtained fully consistent results of $b = 0.923^{+0.019}_{-0.011}$ and $R_p/R_\star = 0.079^{+0.006}_{-0.003}$. The small differences

Table 3. Modelled and derived parameters for TOI-837 b.

Parameter	Prior[a]	Final value[b]
TOI-837 b's parameters		
Orbital period P_{orb} (d)	$\mathcal{U}[8.3239, 8.3259]$	8.3249113 ± 0.0000036
Transit epoch T_0 (BJD$_{TDB}$ − 245 7000)	$\mathcal{U}[2356.77, 2356.87]$	2356.81398 ± 0.00025
Scaled planet radius $R_p/R_\star$	$\mathcal{U}[0.0, 0.2]$	$0.0798^{+0.0032}_{-0.0022}$
Impact parameter b	$\mathcal{U}[0, 1.2]$	$0.920^{+0.011}_{-0.008}$
$\sqrt{e}\cos\omega_\star$	$\mathcal{F}[0]$	0
$\sqrt{e}\sin\omega_\star$	$\mathcal{F}[0]$	0
Doppler semi-amplitude K (m s^{-1})	$\mathcal{U}[0, 100]$	$34.7^{+5.3}_{-5.6}$
GP hyperparameters		
GP period P_{GP} (d)	$\mathcal{U}[2.5, 3.5]$	$2.998^{+0.009}_{-0.010}$
λ_p	$\mathcal{U}[0.1, 5]$	$0.40^{+0.19}_{-0.12}$
λ_e (d)	$\mathcal{U}[1, 100]$	65^{+22}_{-18}
A_{RV} (m s^{-1})	$\mathcal{U}[0, 1000]$	138^{+89}_{-45}
Other parameters		
Stellar density $\rho_\star$ (g cm^{-3})	$\mathcal{U}[0.5, 2.5]$	$1.63^{+0.14}_{-0.15}$
TESS parametrized limb-darkening coefficient q_1	$\mathcal{U}[0, 1]$	$0.875^{+0.091}_{-0.173}$
TESS parametrized limb-darkening coefficient q_2	$\mathcal{U}[0, 1]$	$0.120^{+0.146}_{-0.086}$
El Sauce-*R* parametrized limb-darkening coefficient q_1	$\mathcal{U}[0, 1]$	$0.44^{+0.18}_{-0.14}$
El Sauce-*R* parametrized limb-darkening coefficient q_2	$\mathcal{U}[0, 1]$	$0.41^{+0.30}_{-0.28}$
El Sauce-*I* parametrized limb-darkening coefficient q_1	$\mathcal{U}[0, 1]$	$0.53^{+0.24}_{-0.21}$
El Sauce-*I* parametrized limb-darkening coefficient q_2	$\mathcal{U}[0, 1]$	$0.28^{+0.31}_{-0.20}$
El Sauce-*B* parametrized limb-darkening coefficient q_1	$\mathcal{U}[0, 1]$	$0.42^{+0.24}_{-0.19}$
El Sauce-*B* parametrized limb-darkening coefficient q_2	$\mathcal{U}[0, 1]$	$0.35^{+0.33}_{-0.24}$
ASTEP parametrized limb-darkening coefficient q_1	$\mathcal{U}[0, 1]$	$0.316^{+0.115}_{-0.088}$
ASTEP parametrized limb-darkening coefficient q_2	$\mathcal{U}[0, 1]$	$0.70^{+0.19}_{-0.29}$
Jitter term $\sigma_{TESS,2\,min}$ (ppm)	$\mathcal{J}[1, 5000]$	$205.4^{+75.4}_{-96.5}$
Jitter term $\sigma_{TESS,25\,s}$ (ppm)	$\mathcal{J}[1, 5000]$	248^{+118}_{-145}
Jitter term σ_R (ppm)	$\mathcal{J}[1, 5000]$	1738^{+114}_{-110}
Jitter term σ_I (ppm)	$\mathcal{J}[1, 5000]$	1581^{+191}_{-192}
Jitter term σ_B (ppm)	$\mathcal{J}[1, 5000]$	731^{+478}_{-490}
Jitter term σ_{ASTEP} (ppm)	$\mathcal{J}[1, 5000]$	1311^{+63}_{-62}
HARPS offset (km s^{-1})	$\mathcal{U}[-0.67, 0.71]$	$-0.002^{+0.076}_{-0.073}$
HARPS jitter, σ_{HARPS} (m s^{-1})	$\mathcal{J}[1, 100]$	$26.6^{+3.7}_{-3.3}$
TOI-837 b's derived parameters		
Planet radius (R_J)	...	$0.818^{+0.034}_{-0.024}$
Planet mass (M_J)	...	$0.379^{+0.058}_{-0.061}$
Planet density ρ_p (g cm^{-3})	...	$0.89^{+0.20}_{-0.18}$
Scaled semimajor axis $a/R_\star$	...	$18.16^{+0.50}_{-0.58}$
Semimajor axis a (au)	...	$0.0888^{+0.0026}_{-0.0029}$
Orbital inclination i (°)	...	$87.097^{+0.099}_{-0.129}$
Equilibrium temperature[c] T_{eq} (K)	...	$995.3^{+20.4}_{-19.1}$
Transit duration τ_d (h)	...	$1.983^{+0.034}_{-0.035}$
Planet surface gravity g_p (cm s^{-2})[d]	...	1603^{+377}_{-340}
Planet surface gravity g_p (cm s^{-2})[e]	...	1457^{+302}_{-278}
Insolation F_p (F$_\oplus$)	...	164^{+14}_{-12}

[a]$\mathcal{F}[a]$ refers to a fixed value a, $\mathcal{U}[a, b]$ to an uniform prior between a and b, $\mathcal{N}[a, b]$ to a Gaussian prior with mean a and standard deviation b, and $\mathcal{J}[a, b]$ to the modified Jeffrey's prior as defined by Gregory (2005, equation 16).
[b]Inferred parameters and errors are defined as the median and 68.3 per cent credible interval of the posterior distribution.
[c]Assuming an albedo of 0.
[d]Derived using $g_p = GM_p R_p^{-2}$.
[e]Derived using sampled parameters following Southworth, Wheatley & Sams (2007).
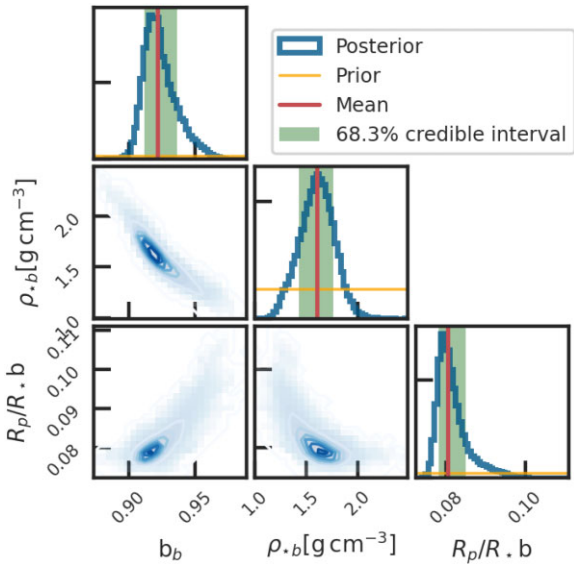
Figure 3. Correlation plot for the main parameters of the transit analysis.

with B20 can be explained by the different ways to deal with the detrending and/or different parametrizations.

We then repeated the analysis including the new data of the *TESS* Cycles 3 and 5. We obtained more precise values of $b = 0.921^{+0.014}_{-0.009}$ and $R_{\rm p}/R_\star = 0.080^{+0.004}_{-0.002}$. These values are still consistent with a grazing transit. Fig. 3 shows a correlation plot between b, $\rho_\star$, and $R_{\rm p}/R_\star$. We can see that the grazing condition covers only the low-probability tail of the posterior distribution. Therefore, we are able to put strong constraints on the inferred planetary radius.

It is also worth mentioning that the stellar density recovered from the transit analysis, $\rho_\star = 1.58 \pm 0.17\ \mathrm{g\,cm^{-3}}$, is fully consistent with the stellar parameters derived in Section 3.1. This suggests that the planetary orbit is nearly circular. To test this further, we performed another transit analysis where we used a Gaussian prior on the stellar density using the value in Table 1. We also sample for the orbit eccentricity using the polar parametrization $\sqrt{e}\cos\omega_\star$ and $\sqrt{e}\sin\omega_\star$. We inferred $\sqrt{e}\cos\omega_\star = 0.08^{+0.12}_{-0.15}$ and $\sqrt{e}\sin\omega_\star = 0.10^{+0.39}_{-0.35}$ that relates to an eccentricity of $e = 0.10^{+0.17}_{-0.06}$. These results are consistent with a nearly circular orbit for TOI-837 b. It is also worth mentioning that the model with a circular orbit is strongly preferred over the model with eccentricity with a difference of Akaike information criterion (ΔAIC) of 52. We then conclude that the photometric data strongly prefer a model assuming a circular orbit. Fig. 4 shows TOI-837 b's transits for the different data sets with the respective inferred models.

3.3 Characterizing the stellar signal

Because of its youth, TOI-837 has strong stellar signals in its light curve and RVs time series. We performed several analyses of the light curves and spectroscopic time series to analyse the time-scales over which the stellar signal evolves.

3.3.1 Stellar signal in the TESS light curves

We first performed a one-dimensional GP regression of the *TESS* light curves to study the behaviour of the stellar signal at the different *TESS* cycles. Since we are interested in modelling the long-term evolution
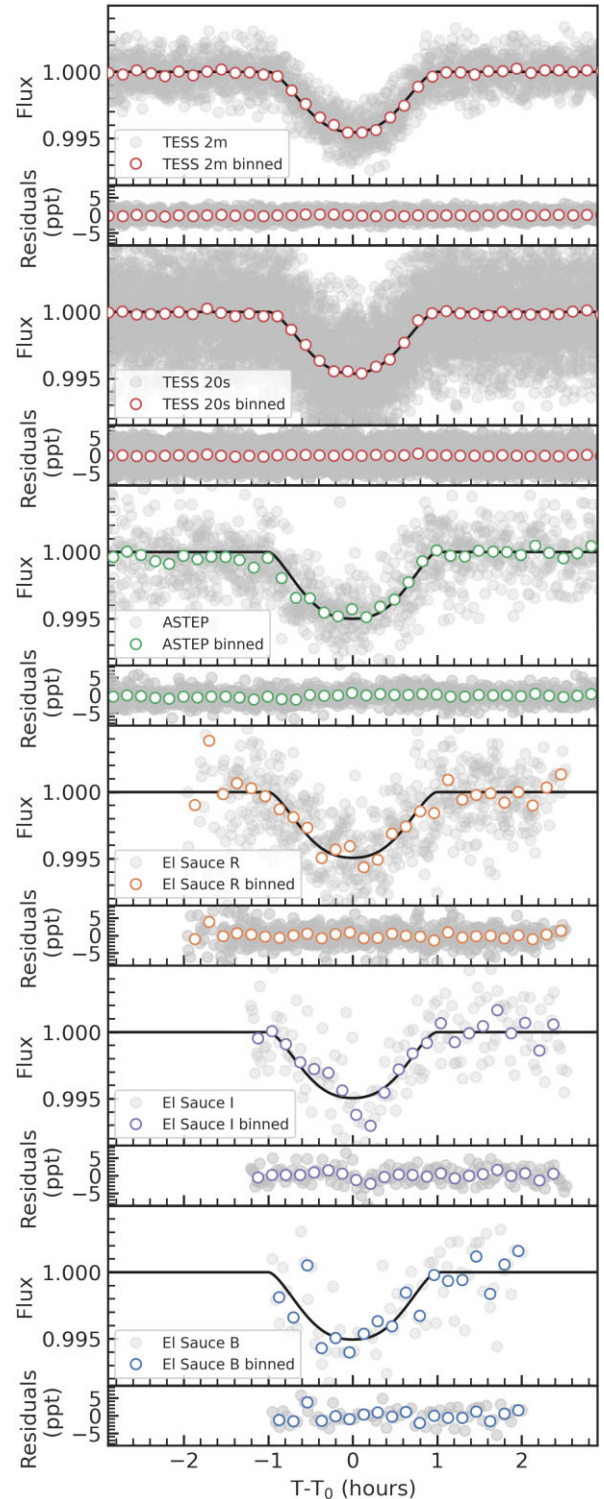
Figure 4. Phase-folded light curves of TOI-837 b for different data sets. Nominal observations are shown in light grey. Coloured circles represent 10-min binned data. Transit models are shown with a solid black line.

of the light curve, we binned the data into 3 h chunks and masked the transits out of the light curve.

We model the covariance between two data points at times t_i and t_j for each time series as

$$\gamma_{\rm 1D} = A^2 \gamma_{i,j}, \tag{1}$$

Table 4. Recovered hyperparameters for one-dimensional GP regression for different stellar time series.

Time series	P_{GP} (d)	λ_e (d)	λ_p
TESS Cycle 1	$2.90^{+0.07}_{-0.03}$	$2.94^{+0.18}_{-0.19}$	$0.43^{+0.03}_{-0.03}$
TESS Cycle 3	$3.09^{+0.05}_{-0.06}$	$2.66^{+0.13}_{-0.12}$	$0.38^{+0.02}_{-0.02}$
TESS Cycle 5	$3.05^{+0.03}_{-0.02}$	$2.50^{+0.11}_{-0.12}$	$0.48^{+0.02}_{-0.02}$
FWHM	3.04 ± 0.02	$10.3^{+4.1}_{-2.6}$	$0.15^{+0.06}_{-0.04}$
BIS span	$2.98^{+0.05}_{-0.02}$	$11.7^{+30.4}_{-6.7}$	$0.13^{+0.04}_{-0.03}$
S_{HK}	3.09 ± 0.03	$44.3^{+35.4}_{-24.9}$	$1.35^{+0.45}_{-0.55}$
Hα	$2.95^{+0.08}_{-0.01}$	$71.8^{+20.8}_{-36.5}$	$0.51^{+0.31}_{-0.21}$

where A is an amplitude term, and $\gamma_{i,j}$ is the QP kernel given by

$$\gamma_{QP,i,j} = \exp\left[-\frac{\sin^2[\pi(t_i - t_j)/P_{GP}]}{2\lambda_P^2} - \frac{(t_i - t_j)^2}{2\lambda_e^2}\right], \quad (2)$$

whose hyperparameters are as follows: P_{GP}, the GP characteristic period; λ_p, the inverse of the harmonic complexity; and λ_e, the long-term evolution time-scale.

We sample five parameters in each run: four GP hyperparameters (A, P_{GP}, λ_e, λ_p), and a jitter term included in the Gaussian likelihood. We set wide uniform priors for all the parameters: for λ_e we set a uniform prior between 0.1 and 100 d, for λ_p between 0.1 and 5, and for P_{GP} between 2.5 and 3.5 d. We sample the parameter space using the built-in MCMC sampler in PYANETI using the same criteria as in Section 3.2.

Table 4 shows the inferred P_{GP}, λ_e, and λ_p hyperparameters for all the light curves. Fig. 5 shows the inferred posterior distributions for the P_{GP}, λ_e, and λ_p parameters for all the modelled time series. Fig. 6 shows the *TESS* light curves with the inferred GP model. The first thing we observe is that the recovered P_{GP} is consistent within the maximum rotational period derived in Section 3.1. However, the rotational period obtained from *TESS* Cycle 1 is consistent with Cycles 3 and 5 just at 3σ. This could be evidence of differential rotation. This can also be caused by the relatively short evolution time-scale recovered that is smaller than the inferred period (see e.g. Rajpaul et al. 2015). We note that all the hyperparameters seem consistent between the different light curves. This is unusual for young stars given that each *TESS* cycle happens 2 yr after another and the evolution of stellar activity can manifest as different signals that can be explained by different GP hyperparameters (e.g. Barragán et al. 2021).

3.3.2 Stellar signal in the activity indicators

We performed an individual analysis of each activity indicator as the one presented in Barragán et al. (2023). We analyse the FWHM, BIS, S_{HK}, and Hα spectroscopic time series. Note that, in comparison with Section 3.3.1, we are now facing a more difficult signal characterization given that the spectroscopic time series are not as well sampled as the *TESS* light curves.

In Section 2.3.1, we show how all the spectroscopic time series periodograms show significant peaks around 3 and 1.5 d, which are related to the stellar rotational period and its first harmonic, respectively. To better characterize the periodic signals and analyse further signal complexity, we performed a GP regression on each time series using the 1D modelling set-up as the one presented in Section 3.3.1. We sample for six parameters in each run, the kernel hyperparameters (A, P_{GP}, λ_e, λ_p), an offset, and a jitter term. The priors used were uniform with the ranges: for λ_e between 0.1
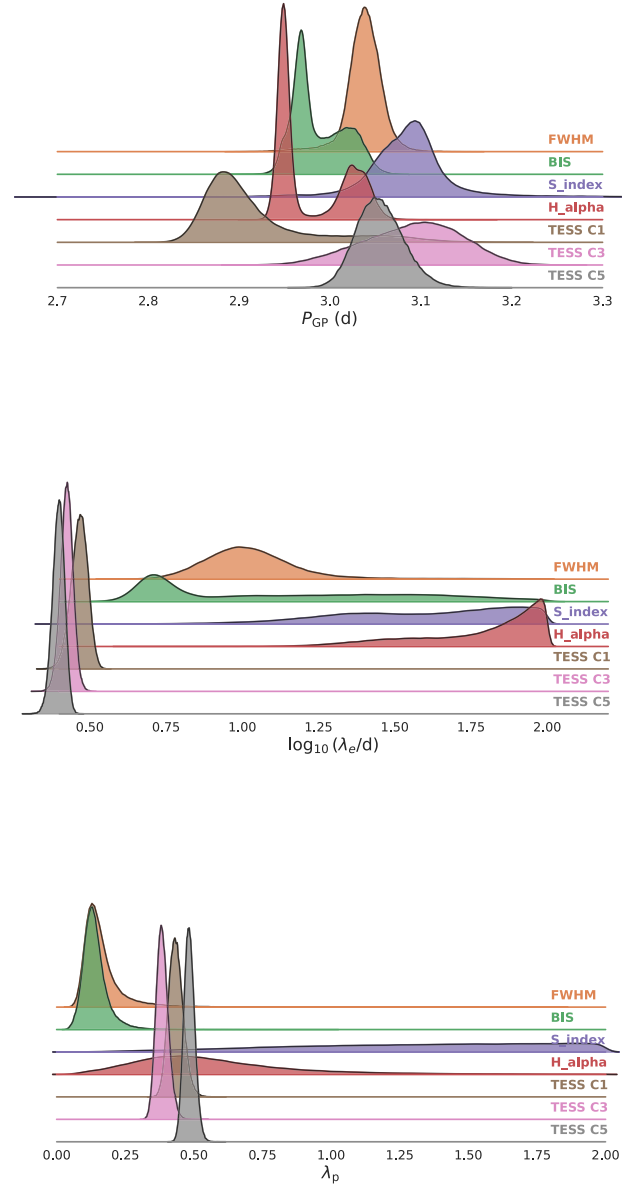
Figure 5. Posterior distributions for P_{GP} (top), $\log_{10}(\lambda_e/d)$ (middle), and λ_p (bottom). Results for FWHM (orange), BIS (green), S_{HK} (purple), Hα (red), and *TESS* Cycles 1 (brown), 3 (pink), 5 (grey) are shown for each subpanel.

and 100 d (that corresponds to the HARPS observing window), λ_p between 0.1 and 2, and for P_{GP} between 2.5 and 3.5 d.

Table 4 and Fig. 5 summarize the inferred GP hyperparameters. Fig. 6 shows the spectroscopic time series data together with the inferred GP model. The first thing we note is that all activity indicators can recover a period that is consistent with the stellar rotation period. This is consistent with the results found in the periodogram analysis (even the double peak observed in the Hα periodogram is presented in the recovered posterior; see Section 2.3.1). We were expecting a better agreement between the hyperparameters recovered from the spectroscopic time series (see Barragán et al. 2023). From Fig. 6 we can see by eye that the recovered process in each time series looks significantly different. The processes
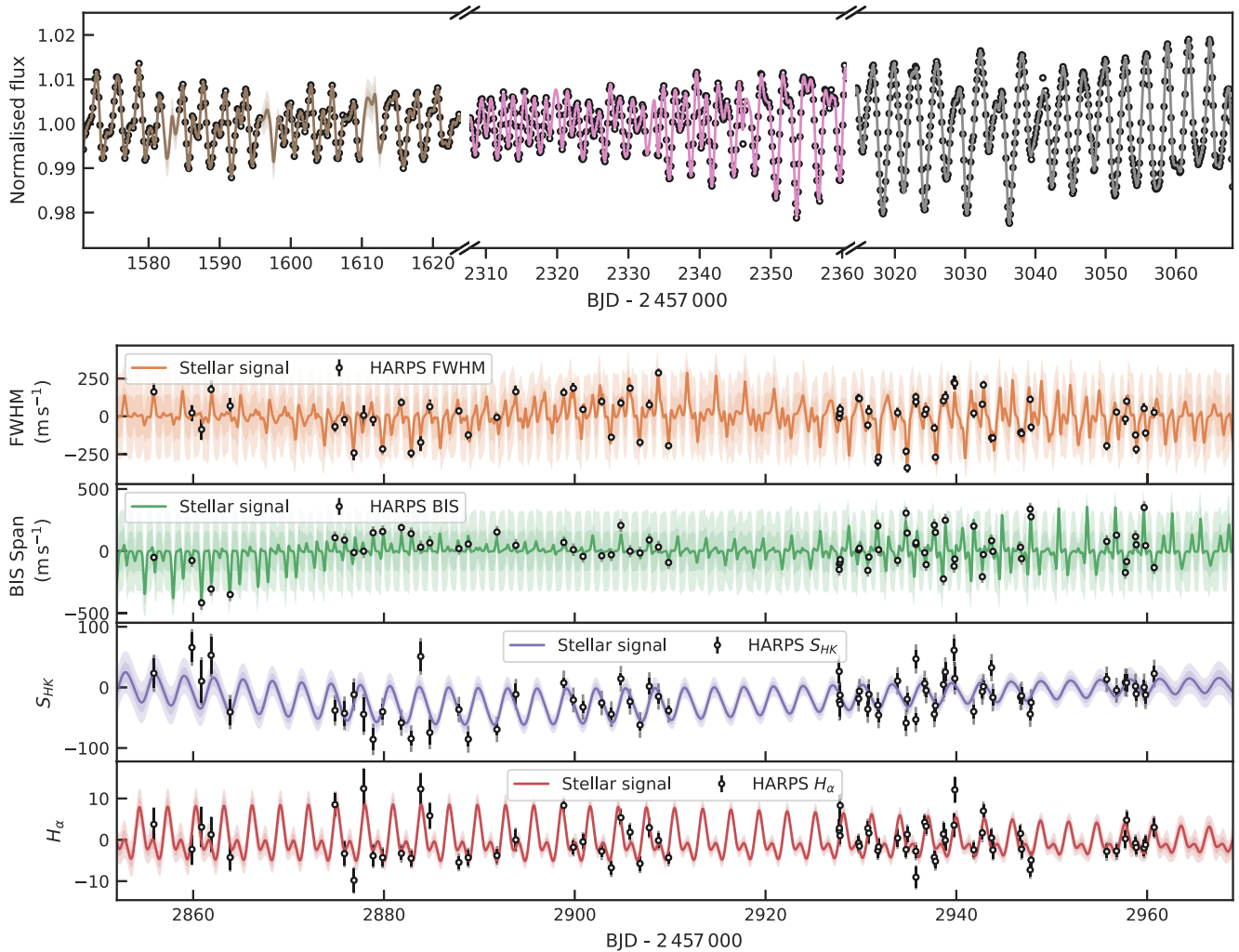
Figure 6. Top panel: TOI-837's *TESS* light curves and GP inferred models. The corresponding measurements (3 h binned data) are shown with black circles. Solid coloured lines show the corresponding inferred signal coming from our GP regression for *TESS* Cycles 1 (brown), 3 (pink), and 5 (grey). Bottom panel: TOI-837 spectroscopic time series for FWHM, BIS span, S_{HK}, and Hα. The corresponding measurements are shown with black circles with error bars with a semitransparent error bar extension accounting for the inferred jitter. Solid coloured lines show the corresponding inferred signal coming from our GP regression, while light coloured shaded areas show the 1σ and 2σ credible intervals of the corresponding GP model.

recovered to explain FWHM and BIS span present variations that are shorter than the time sampling of the HARPS data, this behaviour can be a result of overfitting (see Blunt et al. 2023). We can also see that the recovered signals for S_{HK} and Hα are consistent with a low harmonic complexity process. Barragán et al. (2023) noted that this behaviour can be caused by relatively high white noise that does not allow to characterize the complexity of the underlying signal.

These results suggest that the data cadence is not good enough to characterize the stellar signal in the activity indicators. The rotation period of the star of 3 d is short compared with our sampling strategy of taking one point per night. Three points may not be enough to sample the complexity of the stellar signal, especially if this signal is expected to vary significantly in short time-scales, as suggested by the *TESS* photometry. Therefore, our GP regression may not be able to characterize in full the stellar signal. Furthermore, the rotation period of the star is close to the integer of 3 d. This has as a consequence that observations do not sample properly the phase of the stellar rotation given that observations happen at similar times during the

whole observing run. This is worsened in the case in which the stellar signal evolves drastically between each period.

We conclude that for our spectroscopic time series, we can constrain the rotation period of the star. However, any further complexity pattern that may exist cannot be characterized by our data set. Because of this lack of information on the activity indicators, we conclude that they do not bring enough information of the stellar signal into a multidimensional GP regression analysis. In Appendix A, we show the results and a discussion on the results of applying a multidimensional GP framework to this data set.

3.4 RV analysis

We also performed one-dimensional GP modelling to the RVs time series. We first ran a model identical to the GP analyses in Section 3.3.2. This means that we sample for the QP kernel hyperparameters $(A, P_{GP}, \lambda_e, \lambda_p)$, and a jitter term. As a mean function, we included just an offset (with no Keplerian model yet). For the GP hyperparameters, we use the same priors as the ones described in Section 3.3.2.

We run this analysis for the Gaussian, GND, and GND_2.8 RV time series. For the Gaussian RVs we recover the hyperparameters $P_{\mathrm{GP}} = 3.00 \pm 0.02$ d, $\lambda_e = 42^{+25}_{-16}$ d, and $\lambda_p = 0.39^{+0.22}_{-0.13}$; for GND, $P_{\mathrm{GP}} = 3.00 \pm 0.01$ d, $\lambda_e = 69^{+22}_{-24}$ d, and $\lambda_p = 0.42^{+0.26}_{-0.14}$; and for GND_2.8, $P_{\mathrm{GP}} = 3.00 \pm 0.01$ d, $\lambda_e = 67 \pm 23$ d, and $\lambda_p = 0.42^{+0.25}_{-0.14}$. We can see that the hyperparameters are consistent between the different RV flavours. We can also see that besides the period, the hyperparameters do not compare with any of the hyperparameters obtained from the other spectroscopic time series (see Table 4).

We then repeated the analysis but this time we added a mean function that includes an offset and a Keplerian model to account for the Doppler effect of TOI-837 b. For the planet model we assume a circular orbit, we set Gaussian priors for the planet ephemeris based on the analysis in Section 3.2. For the Doppler semi-amplitude we set a uniform prior between 0 and 100 m s^{-1}. We inferred hyperparameters fully consistent with the no-planet models. We also recovered a Doppler semi-amplitude of $K = 36.6 \pm 6.5$ m s^{-1} for the Gaussian RVs, $K = 34.7 \pm 5.6$ m s^{-1} for the GND RVs, and $K = 34.6 \pm 5.5$ m s^{-1} for the GND_2.8 time series. All these values are fully consistent between them.

When comparing all models, the ones with the planetary signal are strongly favoured with a ΔAIC > 20. It is also worth mentioning that the recovered jitter term for the model with the planet signal is significantly smaller than the one without a Keplerian signal. The jitter values reduce from 38 to 30 m s^{-1}, from 37 to 27 m s^{-1}, and 36 to 26 m s^{-1}, for the Gaussian, GND, and GND_2.8 time series, respectively. This is also evidence that the model that better adjusts the data is the one where the planetary signal is included. The GND_2.8 RV time series yields the most precise Doppler semi-amplitude and exhibits the lowest jitter among the RV series evaluated. Based on these findings, we determine that the GND_2.8 series represents the optimal data set for our analyses. Consequently, we will focus exclusively on this time series in our subsequent work.

3.5 Final joint model

Based on the analyses presented in this section, our final model for the photometric data of TOI-837 is the transit model described in Section 3.2, together with the RV model to the GND_2.8 data described in Section 3.4. For completeness, we ran a final joint model of photometry and RVs to characterize TOI-837 b. The whole set of sampled parameters and priors is shown in Table 3.

We also explored a solution where we allowed for an eccentricity. We inferred an orbital eccentricity of $0.10^{+0.06}_{-0.05}$. However, the model including a circular orbit is slightly preferred with ΔAIC $= 4$. This suggests that the orbit of TOI-837 b is (close to) circular and the data we have are not enough to measure any small deviation from it.

Fig. 7 shows the RV time series, while Fig. 8 shows the phase-folded Doppler signal. Table 3 shows the inferred sampled parameters, defined as the median and 68.3 per cent credible interval of the posterior distribution. Table 3 also shows the derived planetary and orbital parameters.

4 DISCUSSION

4.1 RV detection tests

We know a priori that TOI-837 b exists and its nature is consistent with being planetary (B20). Therefore, we expect that there is a Doppler signal larger than zero that is consistent with the ephemeris

of the transiting signal. If we assumed that TOI-837 b has the same properties as similar planets with its radius, we estimated a mass of $\sim 0.11\,M_{\mathrm{J}}$ that would generate a Doppler signal of ~ 10 m s^{-1} (Chen & Kipping 2017). Due to its youth (~ 35 Myr), we would expect a rather lower density object with a significantly smaller mass (e.g. Fortney, Marley & Barnes 2007; Baraffe, Chabrier & Barman 2008). Our detected Doppler semi-amplitude is $34.7^{+5.3}_{-5.6}$ m s^{-1} that translates to a mass of $0.379^{+0.058}_{-0.061}\,M_{\mathrm{J}}$ for TOI-837 b. This mass together with the inferred radius of $0.818^{+0.034}_{-0.024}\,R_{\mathrm{J}}$ results in a planetary density of $0.89^{+0.20}_{-0.18}$ g cm^{-3}. This unexpected high density on young giant planets has been found previously (Suárez Mascareño et al. 2021), but the RV detection of such planets is challenged by the community (e.g. Blunt et al. 2023). In this section, we test the reliability of our detection of the induced Doppler signal on TOI-837.

#### 4.1.1 Planet signal in periodograms

As shown in Section 2.3.1 and Fig. 2 there is no evidence of the planetary signal in RV GLS periodograms of TOI-837. This is expected given that any planetary signal would be dwarfed by the relatively high stellar activity signal.

We then took the residuals that we obtained from the no-planet one-dimensional GP analyses presented in Section 3.4 for the three different RV time series and we applied GLS periodograms that are shown in the bottom panel of Fig. 2. We can see that the peaks that correspond to the stellar signal disappeared from the periodograms, indicating that the GP model was able to remove the intrinsic stellar signal in the RV time series. Furthermore, a significant peak appeared close to the orbital period of the planet. This result is unexpected. GPs have been proven to engulf planetary signals, especially when the latter ones are not included in the model (e.g. Ahrer et al. 2021; Rajpaul et al. 2021). We speculate that if a relatively strong coherent signal is present in our data set, it may survive a GP regression if it evolves with significantly different time-scales than the stellar signal. This assumption is consistent with the recovered Doppler signal of TOI-837 b.

To explore further the existence of the planetary signal in the periodogram, we ran a $\ell 1$ periodogram (Hara et al. 2017) on the raw GND_2.8 RV time series. Briefly, the $\ell 1$ periodogram is a variation of the Lomb–Scargle periodogram methodology that has reduced sensitivity towards outliers and non-Gaussian noise. Fig. 9 shows the $\ell 1$ periodogram applied to the raw RV time series of TOI-837. The three most significant peak happens at 1.5, 8.31, and 3.09 d that correspond to the first harmonic of the rotation period of the star, the planet orbit, and the rotation period of the star, respectively. This suggests that there is a strong deep-seated signal that coincides with the orbital period of TOI-837 b. This result supports our previous speculation that there is evidence of a strong coherent signal in the RVs that is consistent with our TOI-837 b's recovered Doppler signal.

4.1.2 Cross-validation

The next test we perform is cross-validation to check for overfitting as suggested by Blunt et al. (2023). To do so, we employ a data partitioning strategy similar to the principles of k-fold cross-validation (see e.g. Fazekas & Kovacs 2024) to systematically divide our data set into distinct subsets. Specifically, we first randomized the data set to ensure that each partition is representative of the overall data distribution. Subsequently, we segmented the data set into five partitions. In each iteration, we use four out of these five partitions (constituting approximately 80 per cent of the data) for the
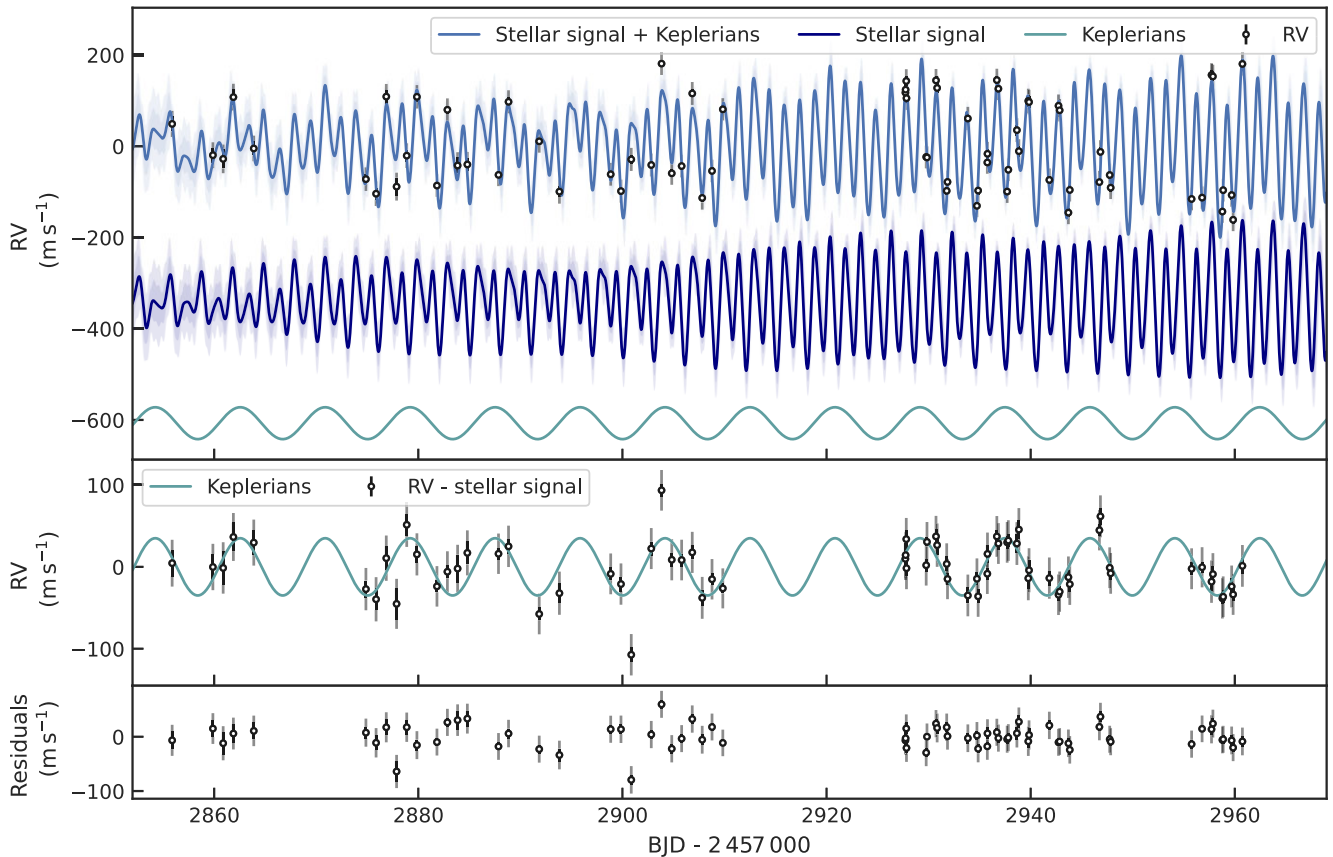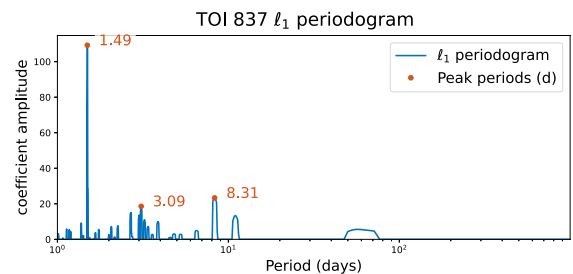
Figure 7. TOI-837's RV time series after being corrected by inferred offsets. Top panel: RV data together with full, stellar and planetary signal inferred models. Measurements are shown with black circles, error bars, and a semitransparent error bar extension accounting for the inferred jitter. The solid lines show the inferred full model coming from our multi-GP, light-shaded areas showing the corresponding GP model's 1σ and 2σ credible intervals. We also show the inferred stellar (dark blue line) and planetary (light green line) recovered signals with an offset for better clarity. Middle panel: RV data with stellar signal model subtracted and planetary model. Bottom panel: RV residuals.
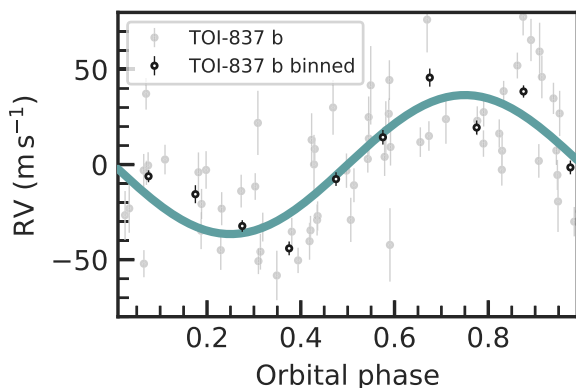
Figure 8. Phase-folded RV signal of TOI-837 b following the subtraction of the systemic velocity and the stellar signal model. The solid line shows the inferred model. Nominal RV observations are shown as light grey points. Solid colourful points show binned data to 1/10 of the orbital phase.

Figure 9. $\ell 1$ periodogram for TOI-837 RVs.

modelling, while the remaining partition (approximately 20 per cent of the data) is masked out. This approach guarantees that each unique subset serves as the test set exactly once, eliminating any potential overlap between masked-out data across all iterations. Fig. 10 shows

the five different subsamples created with this approach.

We then perform an RV analysis (accounting for the planet signal) as the one presented in Section 3.4 for each subsample, we call each one of these runs as subtest i, where i runs between 1 and 5. Fig. 10 shows the data and recovered model for all cases. The recovered Doppler semi-amplitude for each case is fully consistent with the value reported in Section 3.4, but with slightly larger error bars, as expected due to the smaller number of data modelled. We can see that, by eye, the masked-out points fall well within the limits of the inferred models in each case, suggesting that the predictive model in each case can explain the masked-out observations (see also discussion in Luque et al. 2023). We can also see that the predictive
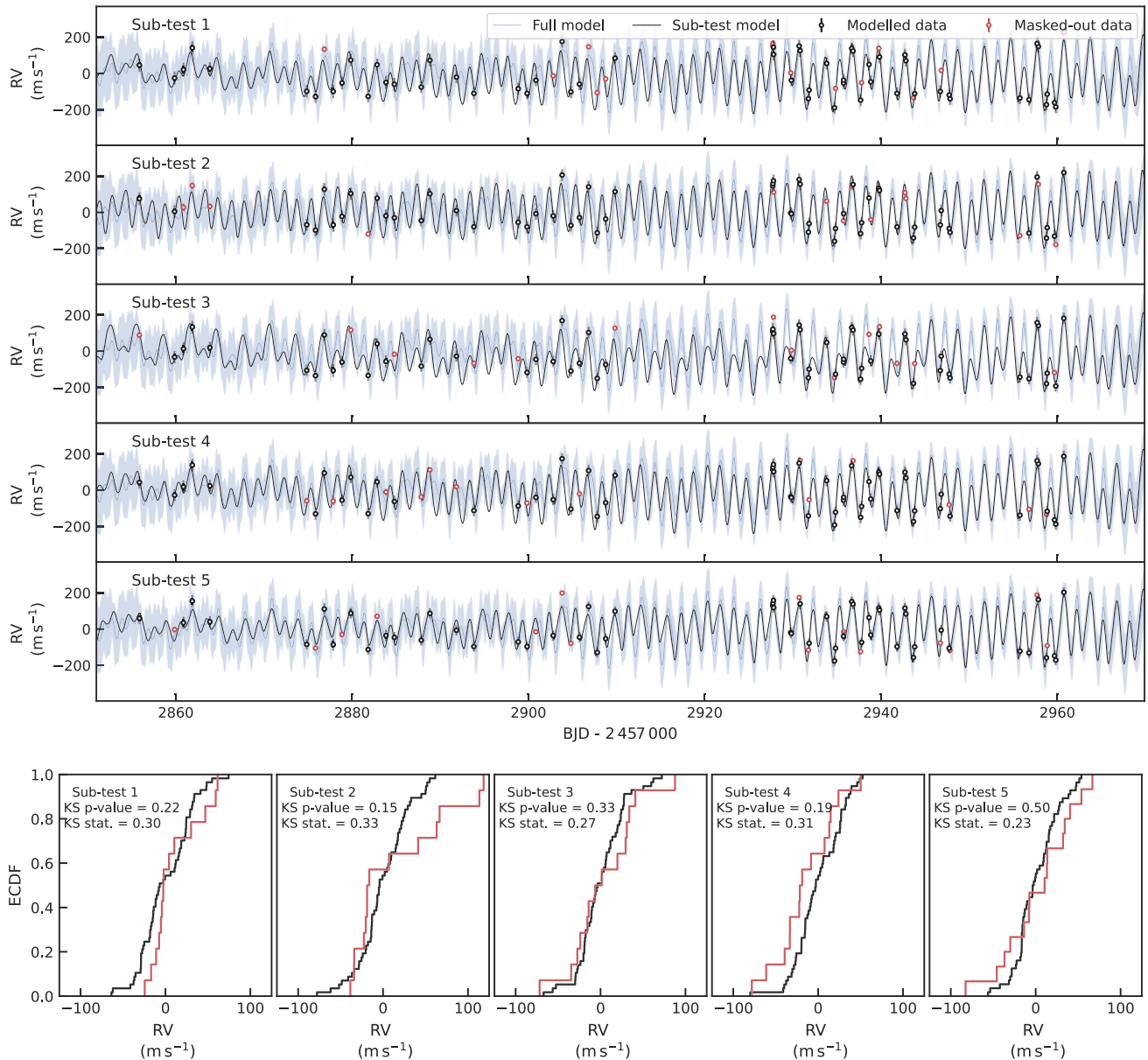
Figure 10. Top panel: Cross-validation results with RV data subsets. Dark circles represent modelled data, red circles indicate masked-out data. The black solid line shows the recovered model for each subtest. We also show the full model and 3σ confidence interval of the full model recovered from the whole data set (same inferred model as Fig. 7) with a blue line and light-shaded areas, respectively. Bottom panel: ECDFs for the residuals of the modelled (black) and masked-out (red) data for all subtests. Each subplot shows the corresponding KS statistics.

model for each subset (black lines) falls well within the confidence intervals of the predictive distribution of the model of the full data set (blue lines and shaded region). These results suggest that our model does not suffer overfitting.

To assess further the reliability of our cross-validation, we perform a two-sample Kolmogorov–Smirnov (KS; Kolmogorov 1933; Smirnov 1948) test. Briefly, the KS test is a non-parametric statistical test that is utilized to validate the hypothesis that two subsets of data originate from the same continuous distribution. This test compares the empirical cumulative distribution functions (ECDFs) of two samples without making any assumptions about the underlying distribution of data. The maximum absolute difference between the ECDFs of the two samples, known as the KS statistic, serves as the basis for evaluating the null hypothesis that the two samples are drawn from the same distribution. A low KS statistic, accompanied by a high *p*-value, indicates a failure to reject the null hypothesis, suggesting that the differences between the two samples could be attributed to random variation, and hence, they can be considered as coming from the same distribution.

We apply the KS test to each one of our subtests in which we compare the residuals of the modelled data with the residuals of the masked-out data (i.e. masked-out points minus predictive distribution at their respective times). If the KS test proves that both samples are explained from the same distribution, then we can conclude that the predictive model explains well the masked-out data. This implies that the inferred model has the ability to explain unseen data, thus,
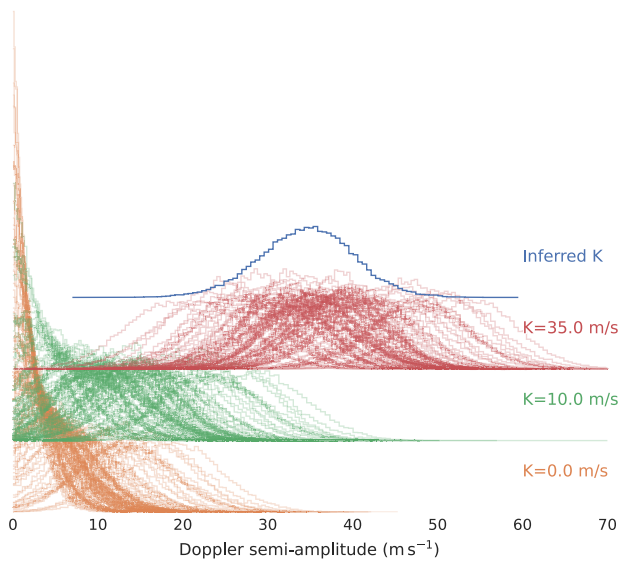
Figure 11. Doppler semi-amplitude distributions from injection tests. The blue line shows results from original data; other coloured lines from synthetic data. Labels indicate injected values.

it does not overfit. Fig. 10 shows the ECDF for the modelled and masked-out data for each one of the subtests. The *p*-values of the five subtests are significantly larger than 0.05, therefore, we can conclude that both samples are consistent with being described by the same underlying distribution. These results give us confidence that our RV model for TOI-837 does not suffer from overfitting.

4.1.3 Injection tests

Previous research indicates that complex models can generate false planet-like RV time series, particularly in stars with high activity levels (e.g. Rajpaul, Aigrain & Roberts 2016). To check if this is our case, we performed injection tests similar to the ones presented in Barragán et al. (2019b) and Zicher et al. (2022). We used CITLALATONAC (Barragán et al. 2022a) to simulate synthetic RV time series at the same time stamps as our HARPS data. We first took the predictive distribution for the stellar signal that we obtained for TOI-837 in Section 3.4. We then added correlated noise using a squared exponential kernel with a length scale of 1 d, and the same amplitude as the jitter term obtained from the real data to simulate the red noise in our data. To finish, we also added white noise for each synthetic observation according to the nominal measurement uncertainty of each HARPS datum. We created 100 different realizations of stellar-like signals. For each stellar-like signal, we created three different types of RV time series injecting signals with Doppler semi-amplitudes of 0 m s^{-1} (assuming there is no planet), 10 m s^{-1} (expected signal of this planet if it were inflated), and 35 m s^{-1} (the recovered signal). This leads to a total of 300 synthetic RV time series with similar noise properties and the same time sampling as the real data.

We model each synthetic data set using a one-planet model and one-dimensional GP configuration as described in Section 3.4. We plot the recovered posterior distribution of the Doppler semi-amplitude of the planet for all the runs in Fig. 11.

We first check the percentage of the simulations in which we can claim a detection. For this purpose, we consider that a detection has

occurred if the median of the posterior is larger than 3σ, where σ is half the interval between the 16.5th and 83.5th percentiles. We found that we can claim a detection of 3, 28, and 100 per cent for the synthetic time series with injected signals of 0, 10, and 35 m s^{-1}, respectively. We then revise which percentage of these detections is consistent with our detection in the real data set. We check what fraction of the time the recovered semi-amplitude in the synthetic time series is within 1σ of the recovered posterior distribution from the real data set. We found that this condition is filled in 0, 1, and 62 per cent of the cases for the 0, 10, and 35 m s^{-1} time series, respectively. These results suggest that if the real Doppler signal presented in our RV time series was 10 m s^{-1}, we would detect the 35 m s^{-1} signal with a probability of 1 per cent. The 62 per cent recovered in the 35 m s^{-1} case is consistent with the expected value taking into account Poisson counting errors.

For the remainder of the paper, we will assume that our mass and radius measurements of TOI-837 b are reliable. Below we describe the physical implications of this for the planet's properties.

4.2 TOI-837 b's properties

With a mass of $0.379^{+0.058}_{-0.061}$ $M_{\rm J}$ and radius of $0.818^{+0.034}_{-0.024}$ $R_{\rm J}$, TOI-837 b's position in the mass–radius diagram is highlighted in Fig. 12. Fig. 12 also shows a mass–radius diagram for giant exoplanets ($0.5 < R_{\rm J} < 2$ $R_{\rm J}$ and $0.1 < M_{\rm p} < 13$ $M_{\rm J}$) detected with a precision better than 30 per cent in radius and mass. Considering that the evolution of planets is influenced by their distance from their host star, we only present planets that orbit within a semimajor axis range of 0.08–1 au. This selection is informed by the semimajor axis of TOI-837 b, ~0.09 au, and is supported by models that forecast a comparable evolution for planets situated within this range of semimajor axes (see Fortney et al. 2007). We also overplot the Fortney et al. (2007)'s models with similar parameters to those of TOI-837 b. This corresponds to models for planets around a solar-like star, with an age of 32 Myr, at a distance of 0.1 au with cores of 25 (pink), 50 (orange), and 100 (green) $M_{\oplus}$. We performed a radial basis function interpolation on the aforementioned Fortney et al. (2007)'s models to find the core mass that best describes the mass and radius of TOI-837 b. We found that the position and age of TOI-837 b would be consistent with a young planet with a core mass of 68 $M_{\oplus}$, assuming a 50–50 per cent ice–silicate core (black line in Fig. 12). This core mass corresponds to ~60 per cent of TOI-837 b total mass of ~125 $M_{\oplus}$.

From Fig. 12, we can see that if well there are planets that fall close to TOI-837 b in the mass versus radius diagram, they all are older than 1 Gyr and they should be compared with older planet's models. This can be done from Fig. 12 where we also show the Fortney et al. (2007)'s models for planets aged 3 Gyr with orbital semimajor axis of 0.1 au. The first thing we see is that the older counterparts of TOI-837 b are consistent with planets with cores $\lesssim$50 $M_{\oplus}$. If TOI-837 b itself was older, we would estimate a significantly smaller core of ~50 $M_{\oplus}$, our estimation of ~70 $M_{\oplus}$ is a pure consequence of the expected inflated state, hence larger radius, given its youth. In this line of thought, TOI-837 b stands out as the only planet with a semimajor axis of ~0.1 au consistent with a ~70 $M_{\oplus}$ core.

We then relaxed our assumptions and proceed to compare TOI-837 b with planets with similar mass and radius, but without constrain on their semimajor axes. We found that K2-60 b (Eigmüller et al. 2017), HD 149026 b (Sato et al. 2005), and TOI-1194 b (Wang et al. 2023) are denser than TOI-837 b and are consistent with core masses between 50 and 100 $M_{\oplus}$ despite being significantly older (>1 Gyr). This suggests that planets with relatively similar masses
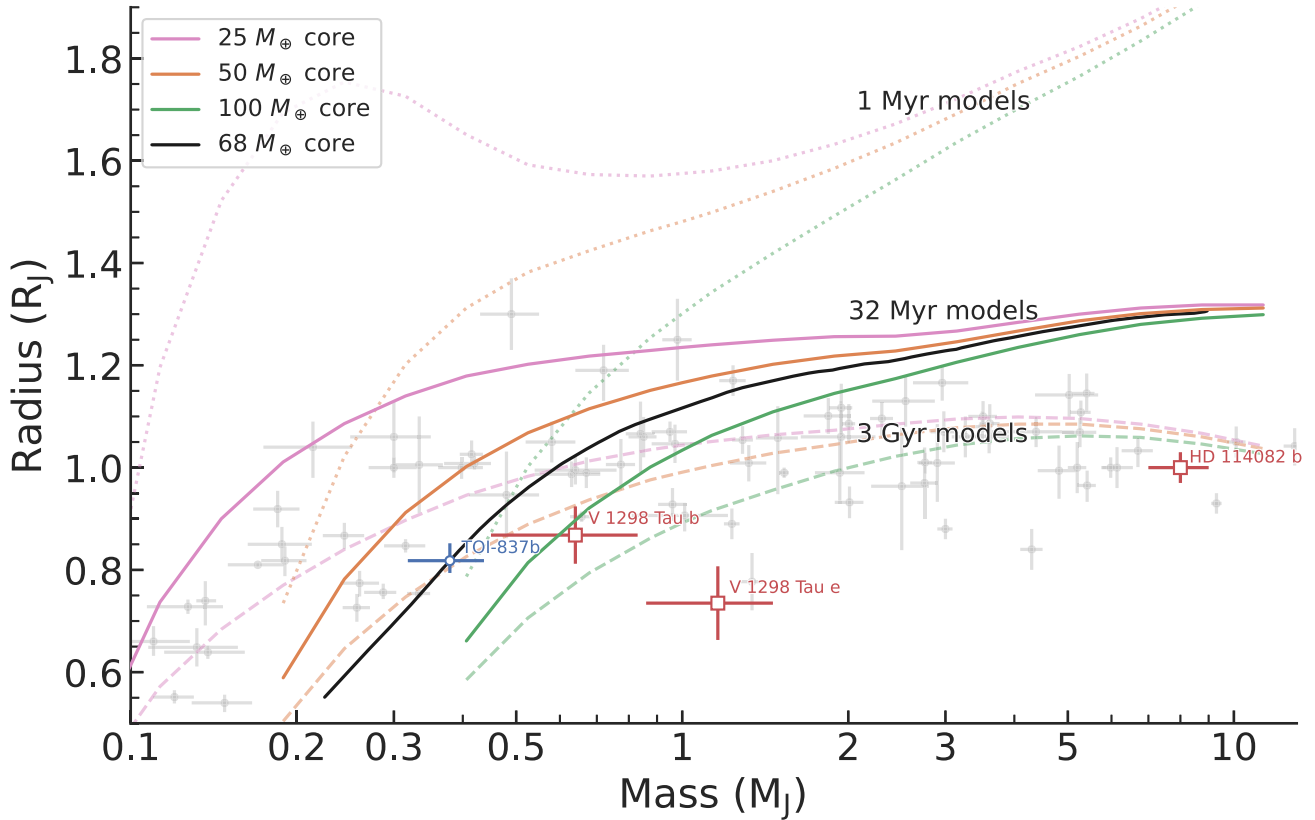
Figure 12. Mass versus radius diagram. Grey data points with error bars show exoplanets with mass and radius measurements with a precision of 30 per cent or better and orbital semimajor axis between 0.08 and 1 au. Data taken from the NASA Exoplanet Archive as of 2024 March (https://exoplanetarchive.ipac.caltech.edu/; Akeson et al. 2013). The location of TOI-837 b is highlighted by a blue circle. Solid lines depict theoretical models predicting the mass–radius relationship for planets of varying core masses, assuming an age of 32 Myr and a distance of 0.1 au from a Sun-like star, based on Fortney et al. (2007). Dotted and dashed lines extend these predictions to planets aged 1 Myr and 3 Gyr, respectively. The black line shows the interpolated model for a 32 Myr old and 68 $M_\oplus$ core. We also highlighted other giant exoplanets younger than 100 Myr with red squares. The methodology for generating this diagram follows the approach outlined in Barragán et al. (2018).

to TOI-837 b and large cores can exist. The question now is what physical mechanisms can create such massive cores. Johnson & Li (2012) theorized that a star's high metallicity might reflect a primordial circumstellar disc with elevated dust content that could potentially enhance core formation. Both HD 149026 b and TOI-1194 b have supersolar atmospheric metallicities that are consistent with this model. In fact, Bean et al. (2023) observed a significant atmospheric metal enrichment on the atmosphere of HD 149026 b that is explained by a bulk heavy element abundance of 66 per cent of the planetary mass. However, the solar metallicity of TOI-837 and K2-60 does not support this hypothesis, suggesting that other factors may also play a critical role in the formation of massive cores. Boley, Granados Contreras & Gladman (2016) proposed a theory where massive cores, with masses exceeding 20 $M_\oplus$, could result from the merging of tightly packed orbiting inner planets that formed during the initial phases of the circumstellar disc's evolution.

Another possibility is that TOI-837 b has a less massive core, but the models are biased towards larger radii for young planets. Core-accretion models of planetary evolution predict planets of <100 Myr to be at the early stages of their contraction phase, showing very large radii and low densities (Fortney et al. 2007; Baraffe et al. 2008, see also 1 Myr models in Fig. 12). However, Fortney et al. (2007)'s models do not include a formation mechanism and can be arbitrarily large and hot at very young ages (see Marley et al. 2007). This can

lead to giant planet models with radii several tenths of a Jupiter radius larger than one computed taking into account formation mechanisms. This would lead as a consequence to estimate more massive cores for a given planet's mass and radius. For the remainder of the paper, we will assume that TOI-837 b can be described by Fortney et al. (2007)'s models assuming a core of 70 $M_\oplus$.

It is also worth to compare TOI-837 b with the properties of other exoplanets that are younger than 100 Myr. According to the NASA Exoplanet Archive (Akeson et al. 2013), there are five such exoplanets documented with precise measurements of age, mass, and radius. These planets include AU Mic b and c (22 Myr; Plavchan et al. 2020; Martioli et al. 2021; Zicher et al. 2022; Donati et al. 2023), V1298 Tau b and e (23 Myr; Suárez Mascareño et al. 2021; Finociety et al. 2023), and HD 114082 b (15 Myr; Zakhozhay et al. 2022). The planets orbiting AU Mic have properties that suggest they are inflated when compared to exoplanets orbiting older stars. This aligns with existing theoretical models that predict younger planets might exhibit such inflated characteristics due to active and intense processes in their early developmental stages. Although these planets are smaller than Neptune, with radii smaller than 4 $R_\oplus$, they showcase a distinct set of physical processes that might differ significantly from those observed in larger exoplanets like TOI-837 b. Moreover, the exoplanets V1298 Tau b and e, along with HD 114082 b, are consistent with giant planets, as illustrated in Fig. 12. Interestingly,
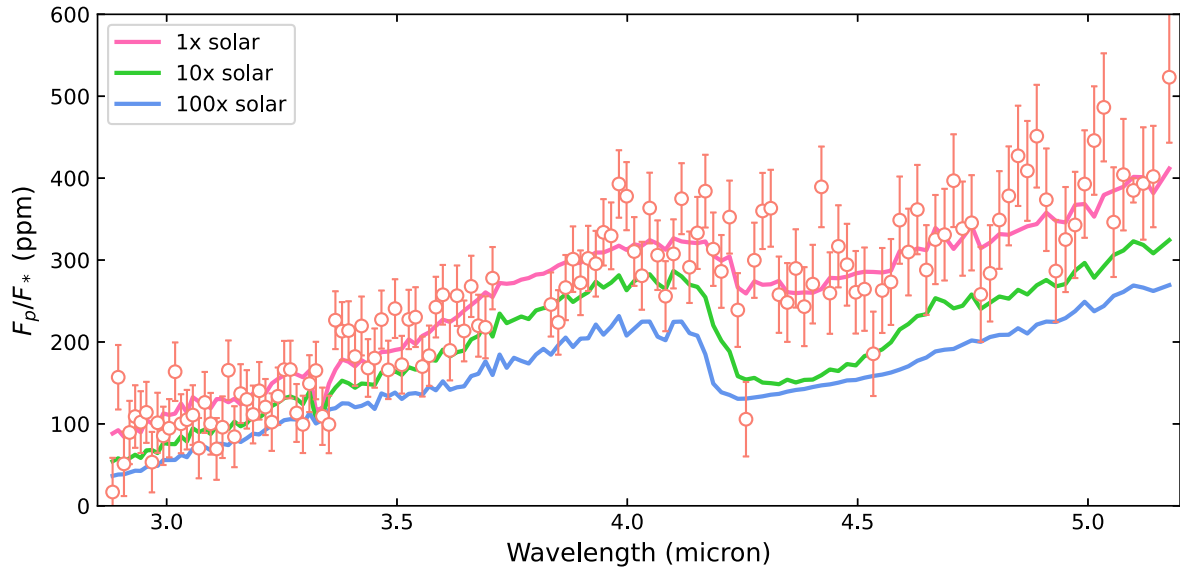
Figure 13. The predicted emission spectrum of TOI-837 b. The red data points show the spectrum attainable with three eclipse observations, using *JWST*/NIRSpec G395H, assuming a solar composition in both metallicity and C/O ratio. For comparison, the forward-modelled spectra assuming 10× and 100× metallicity are also shown (with solar C/O).

these planets are denser than what current theoretical models predict for their age and type (see discussions in Suárez Mascareño et al. 2021; Zakhozhay et al. 2022; Finociety et al. 2023). This tendency suggests that existing theoretical models and/or mass/radius young exoplanet measurements require further dedicated studies. In case our measurement methods are correct, this implies a reconsideration of planetary formation and evolution theories.

4.3 Atmospheric characterization perspectives

Atmospheric observations could play a crucial role in differentiating among various potential formation mechanisms for TOI-837 b. According to the mass–metallicity relationship empirically established by Thorngren et al. (2016), our mass measurement of TOI-837 b suggests a predicted metal fraction ratio between the planet and its host star of $Z_{planet}/Z_{star} = 14.7 \pm 2.5$. With TOI-837's stellar metallicity measured at [Fe/H] = 0.01 ± 0.04, this translates into an estimated bulk metallicity fraction for TOI-837 b of 0.21 ± 0.04. Bean et al. (2023) present a relationship between atmospheric and bulk metallicity fractions. If we assume that TOI-837 b follows this trend, we could expect its atmospheric metallicity to surpass solar values by a factor of 5–8. This significant enhancement in atmospheric metallicity would not only support the substantial core mass inferred from our observations, but also provide insight into the planet's formation conditions and subsequent evolutionary history.

To predict the observability of the atmosphere of TOI-837 b with *JWST*, we leverage packages PICASO[5] and PANDEXO.[6] We forward model the emission spectrum of TOI-837 b using PICASO (Batalha et al. 2019), based on the parameters derived in this work. We make use of the integrated 1D climate modelling for the temperature–pressure (TP) profile and chemical abundance solution (Mukherjee et al. 2023), including all opacities available in PICASO. The TP profile includes a convective zone only in the deepest atmospheric layers. We then use PANDEXO to estimate the S/N of the dayside emission

signal of TOI-837 b with *JWST*/NIRSpec G395H; the predicted observations using three eclipses are shown in Fig. 13, assuming solar metallicity and C/O. At least two eclipse observations are needed to distinguish between a 1× and 10× solar metallicity scenario. Using the chi-square statistic for hypothesis testing, we would expect to distinguish between these cases to a significance of 11.1σ with two eclipse observations (totalling 10.01 h), rising to 17.1σ with three eclipses (Fig. 13). Constraining the atmospheric metallicity will help to break the degeneracy with interior composition and the implications for formation.

5 CONCLUSIONS

Our investigation into the TOI-837 system and its intriguing companion, TOI-837 b, unveils a young Saturn-sized exoplanet that defies conventional expectations with its unexpected massive core. Our exhaustive analysis of data from *TESS* and ground-based observations, and HARPS spectroscopic enabled us to determine TOI-837 b's radius at $0.818^{+0.034}_{-0.024}$ R_J and mass at $0.379^{+0.058}_{-0.061}$ M_J, translating to a density of $0.89^{+0.20}_{-0.18}$ g cm^{-3}. This density together with its age and distance to the star suggests a core mass of approximately 70 $M_\oplus$, accounting for 60 per cent of the planet's total mass. Such a substantial core within a relatively young planetary body presents a challenging scenario for current models of planet formation and core accretion, especially due to the relatively low stellar metallicity.

The unique characteristics of TOI-837 b underscore the urgency for advanced atmospheric characterization. Eclipse observations with *JWST* could to offer unparalleled insights into the composition of TOI-837 b. A measurement of the planetary atmospheric bulk metal fraction will potentially elucidate the true nature of its significant core. Such future studies are crucial for breaking the current degeneracies in planet composition models and could revolutionize our understanding of planetary formation.

We also leave open the possibility that our RV detection could not be accurate. Despite the tailored campaign with a high cadence of observations, the apparent fast evolution of the strong stellar signal could generate biased measurements of the Doppler semi-

[5]https://natashabatalha.github.io/picaso/
[6]https://natashabatalha.github.io/PandExo/index.html

amplitude. We showed with several statistical tests that our RV planetary detection is robust, nevertheless, further observations could help us to test this further. For example, tailored near-infrared RV campaigns, where stellar activity is less significant, with instruments such as the Near Infra Red Planet Searcher (NIRPS) could help to assert our detection in the optical.

DATA AVAILABILITY

The codes used in this paper are freely available at https://github.com/oscaribv. The spectroscopic measurements that appear in Table 2 are available as supplementary material in the online version of this paper. All *TESS* data are available via the MAST archive. Ground-based photometry are available on the online version of Bouma et al. (2020).

REFERENCES

Ahrer E. et al., 2021, MNRAS, 503, 1248
Aigrain S., Foreman-Mackey D., 2023, ARA&A, 61, 329
Aigrain S., Pont F., Zucker S., 2012, MNRAS, 419, 3147
Akeson R. L. et al., 2013, PASP, 125, 989
Ambikasaran S., Foreman-Mackey D., Greengard L., Hogg D. W., O'Neil M., 2015, IEEE Trans. Pattern Anal. Mach. Intell., 38, 252
Astropy Collaboration, 2013, A&A, 558, A33
Astropy Collaboration, 2018, AJ, 156, 123
Astropy Collaboration, 2022, ApJ, 935, 167
Baraffe I., Chabrier G., Barman T., 2008, A&A, 482, 315
Barragán O. et al., 2018, A&A, 612, A95
Barragán O., Gandolfi D., Antoniciello G., 2019a, MNRAS, 482, 1017
Barragán O. et al., 2019b, MNRAS, 490, 698
Barragán O., Aigrain S., Rajpaul V. M., Zicher N., 2022a, MNRAS, 509, 866
Barragán O. et al., 2022b, MNRAS, 514, 1606
Barragán O. et al., 2023, MNRAS, 522, 3458
Barragán O., Aigrain S., Gillen E., Gutiérrez-Canales F., 2021, Res. Notes Am. Astron. Soc., 5, 51
Batalha N. E., Lewis T., Fortney J. J., Batalha N. M., Kempton E., Lewis N. K., Line M. R., 2019, ApJ, 885, L25
Bean J. L. et al., 2023, Nature, 618, 43
Behmard A., Dai F., Howard A. W., 2022, AJ, 163, 160
Blanco-Cuaresma S., 2019, MNRAS, 486, 2075
Blunt S. et al., 2023, AJ, 166, 62
Boley A. C., Granados Contreras A. P., Gladman B., 2016, ApJ, 817, L17
Bouma L. G. et al., 2020, AJ, 160, 239(B20)
Chen J., Kipping D., 2017, ApJ, 834, 17
Cretignier M., 2022, PhD thesis, University of Geneva, Switzerland
Cretignier M., Dumusque X., Allart R., Pepe F., Lovis C., 2020a, A&A, 633, A76
Cretignier M., Dumusque X., Hara N. C., Pepe F., 2021, A&A, 653, A43
Cretignier M., Francfort J., Dumusque X., Allart R., Pepe F., 2020b, A&A, 640, A42
Cutri R. M. et al., 2003, VizieR On-line Data Catalog: II/246
Damasso et al. ., (2024) arXiv e-prints, arXiv:2406.08949
David T. J. et al., 2018, AJ, 155, 222
Donati J. F. et al., 2023, MNRAS, 525, 455
Dotter A., 2016, ApJS, 222, 8
Doyle A. P., Davies G. R., Smalley B., Chaplin W. J., Elsworth Y., 2014, MNRAS, 444, 3592
Eigmüller P. et al., 2017, AJ, 153, 130
Fazekas A., Kovacs G., 2024, preprint (arXiv:2401.13843)
Feroz F., Hobson M. P., Cameron E., Pettitt A. N., 2019, Open J. Astrophys., 2, 10
Finociety B. et al., 2023, MNRAS, 526, 4627
Foreman-Mackey D., Hogg D. W., Lang D., Goodman J., 2013, PASP, 125, 306
Fortney J. J., Marley M. S., Barnes J. W., 2007, ApJ, 659, 1661
Freckelton A. V. et al., 2024, preprint(arXiv:2406.03094)
Gaia Collaboration, 2021, A&A, 649, A1
Gandolfi D. et al., 2018, A&A, 619, L10
Gregory P. C., 2005, ApJ, 631, 1198
Guerrero N. M. et al., 2021, ApJS, 254, 39
Gustafsson B., Edvardsson B., Eriksson K., Jørgensen U. G., Nordlund Å., Plez B., 2008, A&A, 486, 951
Hara N. C., Boué G., Laskar J., Correia A. C. M., 2017, MNRAS, 464, 1220
Harris C. R. et al., 2020, Nature, 585, 357
Heitzmann A. et al., 2021, MNRAS, 505, 4989
Hobson M. J. et al., 2021, AJ, 161, 235
Høg E. et al., 2000, A&A, 355, L27
Howell S. B. et al., 2014, PASP, 126, 398
Hunter J. D., 2007, Comput. Sci. Eng., 9, 90
Jenkins J. M. et al., 2010, in Radziwill N. M., Bridger A., eds, Proc. SPIE Conf. Ser. Vol. 7740, Software and Cyberinfrastructure for Astronomy. SPIE, Bellingham, p. 77400D
Jenkins J. M. et al., 2016, in Chiozzi G., Guzman J. C., eds, Proc. SPIE Conf. Ser. Vol. 9913, Software and Cyberinfrastructure for Astronomy IV. SPIE, Bellingham, p. 99133E
Jenkins J. M., 2002, ApJ, 575, 493
Jenkins J. M., Tenenbaum P., Seader S., Burke C. J., McCauliff S. D., Smith J. C., Twicken J. D., Chandrasekaran H., 2020, Technical Report, Kepler Science Document KSCI-19081-003, id. 9
Johnson J. L., Li H., 2012, ApJ, 751, 81
Kipping D. M., 2013, MNRAS, 435, 2152
Kolmogorov A., 1933, Giorn. Ist. Ital. Attuari, 4, 83
Kurucz R. L., 1993, SYNTHE Spectrum Synthesis Programs and Line Data. Kurucz CD-ROM No. 18. Smithsonian Astrophysical Observatory, Cambridge, MA
Li J., Tenenbaum P., Twicken J. D., Burke C. J., Jenkins J. M., Quintana E. V., Rowe J. F., Seader S. E., 2019, PASP, 131, 024506
Lovis C., 2007, PhD thesis, University of Geneva, Switzerland
Luque R. et al., 2023, Nature, 623, 932
Mallorquín M. et al., 2023, A&A, 680, A76
Mandel K., Agol E., 2002, ApJ, 580, L171
Mann A. W. et al., 2022, AJ, 163, 156
Mantovan G. et al., 2024, A&A, 682, A129
Marley M. S., Fortney J. J., Hubickyj O., Bodenheimer P., Lissauer J. J., 2007, ApJ, 655, 541

[7] http://www.astropy.org

Martioli E., Hébrard G., Correia A. C. M., Laskar J., Lecavelier des Etangs A., 2021, A&A, 649, A177

Mayor M. et al., 2003, The Messenger, 114, 20

Mortier A. et al., 2020, MNRAS, 499, 5004

Morton T. D., 2015, Astrophysics Source Code Library, record ascl:1503.011

Mukherjee S., Batalha N. E., Fortney J. J., Marley M. S., 2023, ApJ, 942, 71

Plavchan P. et al., 2020, Nature, 582, 497

Rajpaul V. M. et al., 2021, MNRAS, 507, 1847

Rajpaul V., Aigrain S., Osborne M. A., Reece S., Roberts S., 2015, MNRAS, 452, 2269

Rajpaul V., Aigrain S., Roberts S., 2016, MNRAS, 456, L6

Ricker G. R. et al., 2015, J. Astron. Telesc. Instrum. Syst., 1, 014003

Rizzuto A. C. et al., 2020, AJ, 160, 33

Sato B. et al., 2005, ApJ, 633, 465

Smirnov N., 1948, Ann. Math. Stat., 19, 279

Smith J. C. et al., 2012, PASP, 124, 1000

Southworth J., Wheatley P. J., Sams G., 2007, MNRAS, 379, L11

Stumpe M. C. et al., 2012, PASP, 124, 985

Stumpe M. C., Smith J. C., Catanzarite J. H., Van Cleve J. E., Jenkins J. M., Twicken J. D., Girouard F. R., 2014, PASP, 126, 100

Suárez Mascareño A. et al., 2021, Nat. Astron., 6, 232

The Pandas Development Team, 2020, pandas-dev/pandas: Pandas. Zenodo (https://doi.org/10.5281/zenodo.3509134)

Thorngren D. P., Fortney J. J., Murray-Clay R. A., Lopez E. D., 2016, ApJ, 831, 64

Tsantaki M., Andreasen D., Teixeira G., 2020, J. Open Source Softw., 5, 2048

Tsantaki M., Sousa S. G., Adibekyan V. Z., Santos N. C., Mortier A., Israelian G., 2013, A&A, 555, A150

Twicken J. D. et al., 2018, PASP, 130, 064502

Wang J.-Q. et al., 2023, preprint (arXiv:2310.12458)

Winn J. N., 2010, in Seager S., ed., Exoplanets. Univ. Arizona Press, Tucson, AZ, p. 55

Zakhozhay O. V. et al., 2022, A&A, 667, L14

Zechmeister M., Kürster M., 2009, A&A, 496, 577

Zicher N. et al., 2022, MNRAS, 512, 3060

SUPPORTING INFORMATION

Supplementary data are available at *MNRAS* online.

Table 2. HARPS spectroscopic measurements.

Please note: Oxford University Press is not responsible for the content or functionality of any supporting materials supplied by the authors. Any queries (other than missing material) should be directed to the corresponding author for the article.

APPENDIX A: MULTIDIMENSIONAL GP ANALYSIS

In Section 3.3, we performed an analysis of different activity indicator time series (as in Barragán et al. 2023). We found that they do not contain significant information about the stellar signal, more than the period. Therefore, we conclude that they do not bring enough information that can help us to constrain better the shape of the stellar signal in the RV time series within a multidimensional GP framework.

As an educational test, we perform a two-dimensional GP analysis between the RV and FWHM time series. We follow the framework of Rajpaul et al. (2015) and Barragán et al. (2022a) where we assume that RVs and FWHM are modelled as

$$
\begin{aligned}
\text{RV} &= A_{\text{RV}} G(t) + B_{\text{RV}} \dot{G}(t), \\
\text{FWHM} &= A_{\text{FWHM}} G(t),
\end{aligned} \tag{A1}
$$

where the variables A_{RV}, B_{RV}, and A_{FWHM} serve as free parameters that connect the individual time series with $G(t)$ and $\dot{G}(t)$. Here, $G(t)$ is considered a latent variable, meaning it is not directly observed. This variable can be broadly understood as representing the portion of the visible stellar disc that is covered by active regions over time.

We performed a multidimensional GP repression using PYANETI and the same MCMC set-up described in Section 3.2. We model the GND_2.8 RVs together with the FWHM. We use the QP kernel given in equation (2) to construct the covariance matrix. The mean function for the FWHM was assumed to be an offset while for the RV was including a Keplerian following the guidelines presented in Section 3.4. All priors follow the same guidelines presented in Table 3.

The recovered GP hyperparameters are $\lambda_e = 13.9^{+4.1}_{-3.4}$ d, $\lambda_p = 0.46^{+0.11}_{-0.08}$, and $P_{\text{GP}} = 3.01 \pm 0.02$ d. The period is fully consistent with the results presented in Section 3.4, as expected. We can see that the λ_p is relatively larger than the value reported in Table 3. This is also expected given that in the multidimensional GP analysis, the high harmonic complexity in the RV time series is absorbed by the derivative term, $\dot{G}$, used to model the RVs (see discussions in Barragán et al. 2022a, b, 2023). On the other side, λ_p is also larger than the value recovered from the FWHM one-dimensional analysis (see Table 4). This is not expected given that in both analyses we would expect that the FWHM constrains a similar shape and behaviour of the underlying $G(t)$ process. The relatively high harmonic complexity found in Section 3.3.2 is likely caused by an overfitting that makes the model of the FWHM to vary faster than the sampling of the HARPS data. The lower harmonic complexity found in this case can be attributed to the RV time series setting a constrain on the shape of $G(t)$. In Fig. A1, we can see how the FWHM time series looks better constrained than the signal recovered in Fig. 6. We also obtain a $\lambda_e = 13.9^{+4.1}_{-3.4}$ d that is smaller than the value obtained in the one-dimensional RV analysis but similar to the value found in the FWHM analysis. This suggests that in this case, the FWHM constrains the evolutionary time-scale. This has sense given that it is expected that a shorter time-scale will dominate the evolutionary parameter of two signals with different λ_e values. From this analysis, we can deduce that the multidimensional GP approach is able to model the stellar signal in the RV and FWHM time series. In this case, the RV time series allows to guide the shape of the $G(t)$ that permits a better modelling of the stellar signal in the FWHM time series. We perform another run when we model the Gaussian fit RVs and we obtained fully consistent results.

Regarding the planetary signal, we recover $K = 35.0 \pm 5.4$ m s^{-1} that translates into a mass of $0.391 \pm 0.064\, M_{\text{J}}$. These values are fully consistent and almost identical with the ones presented in Section 3.4 and Table 3. For a fit using the Gaussian fit RVs we recover $K = 36.4 \pm 5.9$ m s^{-1} that translates into a mass of $0.391 \pm 0.064\, M_{\text{J}}$. We note that these results do not bring any significant improvement with respect to the one-dimensional GP model presented in Section 3.4 (see also Barragán et al. 2023). This can be explained by the lack of information in the activity indicators. Therefore, we have chosen to adopt the more conservative one-dimensional regression approach for the main paper. This decision is driven by our judgment regarding the use of an activity indicator that alone does not constrain the stellar signal.
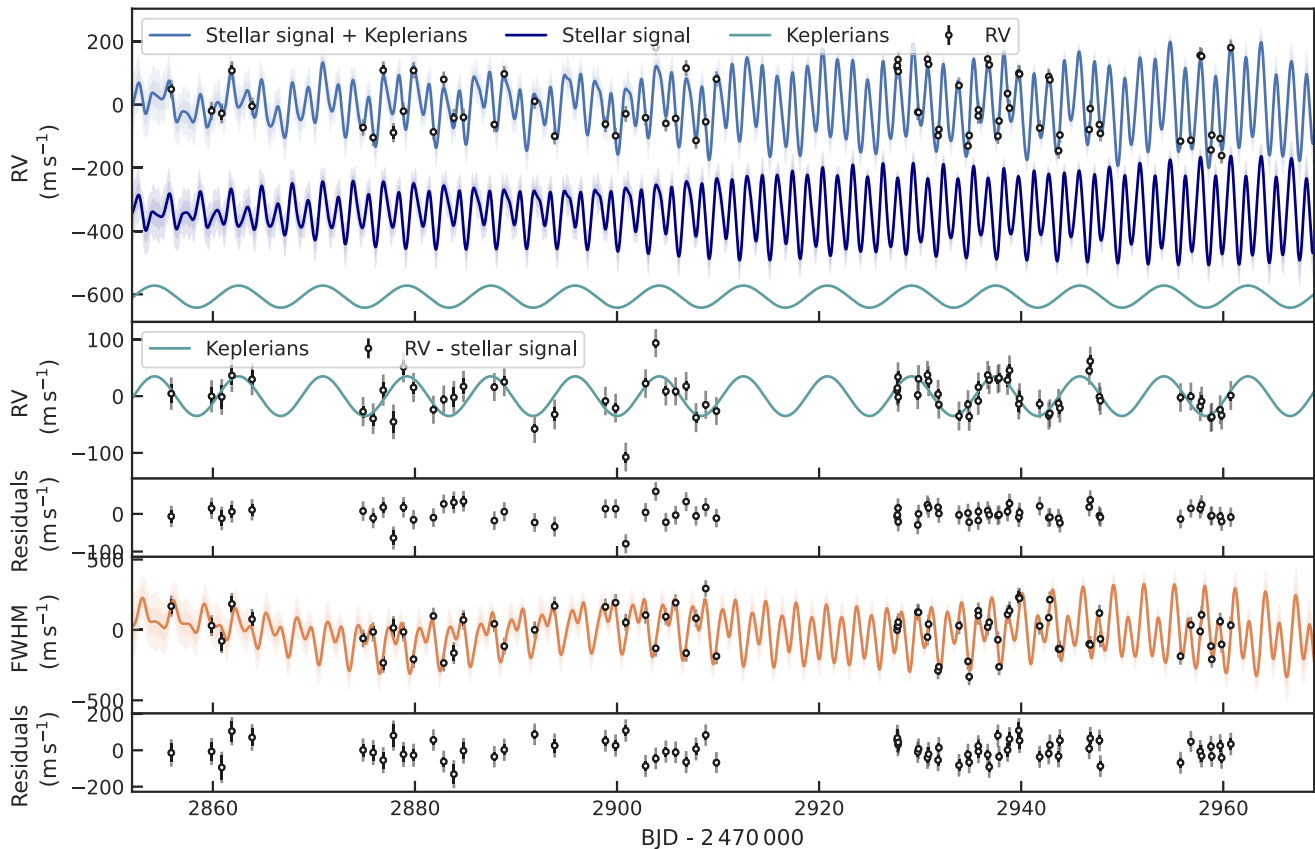
Figure A1. TOI-837's RV and FWHM time series after being corrected by inferred offsets. The plot shows (from top to bottom) RV data together with full, stellar and planetary signal inferred models; RV data with stellar signal model subtracted; RV residuals; FWHM data together with inferred stellar model; and FWHM residuals. Measurements are shown with black circles, error bars, and a semitransparent error bar extension accounting for the inferred jitter. The solid lines show the inferred full model coming from our multi-GP, light-shaded areas showing the corresponding GP model's 1σ and 2σ credible intervals. For the RV time series (top panel), we also show the inferred stellar (dark blue line) and planetary (light green line) recovered signals with an offset for better clarity.

This paper has been typeset from a TEX/LATEX file prepared by the author.